Published in final edited form as:
*Neuroimage*. 2014 Oct;100:176-91. doi: 2014. DOI: 10.1016/j.neuroimage.2014.06.015

# Beyond Fractional Anisotropy: Extraction of Bundle-Specific Structural Metrics from Crossing Fiber Models

Till W. Riffert[a], Jan Schreiber[a], Alfred Anwander[b], Thomas R. Knösche[a]*

[a] Research & Development Unit "MEG & Cortical Networks and Cognitive Functions", Max Planck Institute for Human Cognitive and Brain Sciences, Leipzig, Germany.

[b] Department of Neuropsychology, Max Planck Institute for Human Cognitive and Brain Sciences, Leipzig, Germany.

* Address for correspondence:

Thomas R. Knösche
Max Planck Institute for Human Cognitive and Brain Sciences
Stephanstrasse 1a, 04103 Leipzig, Germany.
http://www.cbs.mpg.de/~knoesche
phone: +49 341 9940 2619

## Abstract

Diffusion MRI (dMRI) measurements are used for inferring the microstructural properties of white matter and to reconstruct fiber pathways. Very often voxels contain complex fiber configurations comprising multiple bundles, rendering the simple diffusion tensor model unsuitable. Multi-compartment models deliver a convenient parameterization of the underlying complex fiber architecture, but pose challenges for fitting and model selection. Spherical deconvolution, in contrast, very economically produces a fiber orientation density function (fODF) without any explicit model assumptions. Since, however, the fODF is represented by spherical harmonics, a direct interpretation of the model parameters is impossible. Based on the fact that the fODF can often be interpreted as superposition of multiple peaks, each associated to one relatively coherent fiber population (bundle), we offer a solution that seeks to combine the advantages of both approaches: first the fiber configuration is modeled as fODF represented by spherical harmonics and then each of the peaks is parameterized separately in order to characterize the underlying bundle. In this work, the fODF peaks are approximated by Bingham distributions, capturing first and second order statistics of the fiber orientations, from which we derive metrics for the parametric quantification of fiber bundles. We propose meaningful relationships between these measures and the underlying microstructural properties. We focus on metrics derived directly from properties of the Bingham distribution, such as peak length, peak direction, peak spread, integral over the peak, as well as a metric derived from the comparison of the largest peaks, which probes the complexity of the underlying microstructure. We compare these metrics to the conventionally used fractional anisotropy (FA) and show how they may help to increase the specificity of the characterization of microstructural properties. While metric relying on the first moments of the Bingham distributions provide relatively robust results, second-order metrics representing the peak spread are only meaningful, if the SNR is very high and no fiber crossings are present in the voxel.

## Keywords

Diffusion MRI, spherical deconvolution, microstructural metrics, Bingham distribution, fiber orientation density function

## Introduction

Using diffusion MRI (dMRI), the mean local orientation distribution of nerve fibers in the white matter of the brain within a voxel (size 1-30 $mm^3$) can be probed (Le Bihan et al., 1986). This information on the local fiber layout can then be used to compute fiber pathways through the white matter (tractography; Conturo et al., 1999, Mori and van Zijl, 2002, Behrens et al., 2003), or to derive measures characterizing the state of the tissue, which can in turn be used to detect changes and differences related to, for example, development, aging, disease, learning, and cognitive performance (for an overview, see Jones et al., 2013).

### *Local models*

In order to draw conclusions on the underlying fiber structure from the measured diffusion weighted signal, it is necessary to impose a model connecting anatomy and diffusion signal. This is called the local model, because it describes the influence of the local microstructural boundaries within a voxel on the spatial displacement of water molecules (i.e., diffusion) in that voxel, and it also describes the influence on the measured signal from that voxel. In many cases, approximations of the average water diffusion propagator $p(r,t)$ in the voxel are constructed. This function gives the ensemble averaged probability of a water molecule traveling the distance r within time t (Cory and Garroway, 1990, Callaghan et al., 1991). It is related to the underlying tissue structure by the diffusion equation and the appropriate boundary conditions. In practice, probing the diffusion propagator is constrained by sensitivity of the measurement with respect to diffusion direction, governed by the diffusion gradients, and diffusion time and length, expressed by the b-value. Both together they form the so-called q-space. In the simplest case one assumes anisotropic Gaussian diffusion, which leads to a diffusion propagator that can be approximately described by a tensor. This technique is called diffusion tensor imaging (DTI) (Basser et al., 1994) and is appropriate in situations with only one, approximately coherent, fiber population per voxel. One of the obvious limitations of this method lies in its inability to resolve the micro-structure in areas of more complex fiber geometries, for example crossing fibers. This situation is rather common and affects, at the current resolutions, between one and two thirds of all white matter voxels (Behrens et al., 2007, Descoteaux, 2008, Jeurissen et al., 2010). In order to cope with this problem, two different principled approaches have been pursued.

The first approach is to construct multi-compartment models, such as the ball-and-stick model (Behrens et al., 2007) and various multiple tensor models (Tuch et al., 2002, Alexander, 2005). They seek to decompose the diffusion propagator into a number of sub-components, each associated with an underlying roughly collinear fiber bundle. Alternatively, one can also try to model the fiber density of the bundles directly, for example by representing the angular fiber density of each bundle by a Bingham or

Watson distribution and then convolve it with the (assumed) signal of a single fiber (Kaden et al., 2007; Zhang et al., 2012; Sotiropoulos et al., 2012).

As long as the assumption holds that the fibers belong to a small and known number of fairly coherent bundles, these methods are very attractive, because they separate multiple fiber populations, while each of them can be described by simple and descriptive parameters. However, a generalized model allowing any number of compartments leads to numerical problems. In the work of Scherrer and Warfield (Scherrer and Warfield, 2010), it has been shown for the multiple tensor model that these problems stem from the colinearity of the parameters. Therefore a single b-value is insufficient for estimating the full model of multiple tensors. Attempts to solve this problem include restricting the number of tensor components (eg. to two components, Parker et al., 2003, Caan et al., 2010), incorporating physiological constraints (Tuch et al., 2002), reducing the complexity of the model by only allowing identical prolate tensors (Tabelow et al., 2012), stabilizing the problem by using Monte-Carlo algorithms (Kreher et al., 2005), regularizing over a spatial neighborhood (Pasternak et al., 2008, Malcolm et al., 2010), and incorporating other local models to estimate the initial non-linear optimization of the parameters of the multi-tensor model (Schultz and Kindlmann, 2010).

The second principled approach to complex fiber configurations involves fewer model assumptions by approximating either the angular structure of the diffusion propagator or directly the fiber orientation distribution by a set of orthonormal basis functions, usually spherical harmonics (SH). These methods do not require any prior assumptions on the number of underlying fiber bundles. They include Q-Ball Imaging (Tuch, 2004, Barnett, 2009, Canales-Rodríguez et al., 2009, Tristán-Vega et al., 2009, Aganj et al., 2010) approximating the diffusion orientation density function (dODF) and Spherical Deconvolution (SD) (Tournier et al., 2004, Dell'Acqua et al., 2007, Kaden et al., 2007, Tournier et al., 2007) modeling the fiber orientation density function (fODF). The fODF represents the direction dependent density of fibers in every voxel and therefore is an angular spatial fiber density. If viewed for a given voxel it represents a measure of the angular fiber density. Calculating the fODF requires an estimate of the signal attenuation generated by a single fiber bundle, the so-called deconvolution kernel. A common framework for the different approaches to spherical deconvolution is given by Jian and Vermuri (2007).

While the SH representations of dODF and fODF allow for a very parsimonious parameterization, which can be very efficiently estimated from the data, the parameters do not usually bear any direct meaning. This makes direct interpretation in terms of fiber properties, such as mean directions and spreadings of the particular fiber populations, unwieldy. Additionally, the SH representation does not allow for separate characterization of the different fiber bundles present in one voxel, since these are part of the multimodal distribution structure represented by the SH.

In order to keep the advantages of SH based ODF models and at the same time profit from more descriptive parameterizations of fiber bundles, we propose to separately

characterize the peaks of the fODF by Bingham distributions (Bingham, 1974). This distribution can be seen as an axial Gaussian distribution on a unit sphere (Mardia, 1975). As mentioned above, it has been already used in multi-compartment models for the characterization of fiber bundles (Kaden et al., 2007; Zhang et al., 2012; Sotiropoulos et al., 2012). By fitting each relevant peak in the fODF with a Bingham distribution we obtain a bundle-wise characterization of the fiber density without having to re-introduce multi-compartment models with their larger parameter spaces and inherent model selection problems. In our approach, if one increases or decrease the number of relevant peaks (by changing the criteria for 'relevance'), the characterization of the other bundles will not be affected. The method therefore is a way to characterize the features of the widely used fODF, rather than a local model of its own.

## *Metrics*

Metrics describe distances in a parameter space and are characterized by their sensitivity and specificity towards the differences in the physical quantities they are meant to reflect. In the context of dMRI, a sensitive metric should react to differences in a wide range of microstructural properties of the tissue. A metric fulfilling this requirement is the fractional anisotropy (FA) (Basser, 1995), which is based on the diffusion tensor's geometry. For example, the anisotropy in a region may be lower because of a reduction in myelination or an increase in the variance of fiber orientation, but also because there is a larger axon diameter, a lower packing density (Takahashi et al., 2002) – both of which denote fewer barriers to diffusion in a given space – or it could be due to increased membrane permeability (reducing the effectiveness of a boundary). However, with this sensitivity the FA loses specificity. In other words, one is not able to determine the particular type of microstructural change simply from a change in FA. Other measures derived from the tensor, such as radial, axial and mean diffusivity have also been shown to correlate with microstructural properties. However, so far it has not been possible to find a robust, quantitative relationship between a single microstructural property and parameters extracted from the tensor (Jones et al., 2013). Although the limited amount of acquired data makes it impossible to achieve absolute specificity, the fact that the tensor represents only part of the available information in the data gives reason for hope that more specific metrics than FA might be possible. Such metrics should be designed to improve the situation in one of the following two ways: First, they reproduce results which are also uncovered by FA, thus endowing them with additional meaning. In other words, the fact that a new metric shows the same differences as the FA may tell us something about the possible origin of the FA changes, thereby increasing specificity. Second, the metrics uncover microstructural changes, which are not seen in FA, thus increasing sensitivity. Since the FA is very sensitive but not very specific in its nature, we expect to mostly encounter the former situation.

Alternative metrics to FA have been introduced based on more complex local models. The most prominent of these is the generalized FA (GFA) (Tuch, 2004). Here the definition of the FA is extended to the q-ball by using the quotient of standard deviation and root mean square of the dODF instead of the tensor. While GFA is a global measure in each voxel, Ghosh and Deriche (2011) introduced a bundle specific metric using a polynomial approach in order to represent the dODF and extracted geometric information to define a peak FA. Similarly, Raffelt et al. (2012b) as well as Dell'Acqua et al. (2013) introduced the length of an fODF peak as bundle specific metric.

It should be noted that, while these metrics are endowed with additional meaning, they are still based on the information which can be extracted from the diffusion models. Therefore they are clearly limited in the insights they can provide. True biophysical metrics have to be derived from local models of fibers, such as the fODF computed with SD. Even more sophisticated models that describe properties beyond fiber density are usually based on specialized acquisition schemes especially varying gradient strength and/or diffusion time resulting in long acquisition times (Assaf and Basser, 2005, Alexander et al., 2010 ).

Here, we explore several metrics derived directly from the Bingham distributions used to characterize the fODF and with it the tissue microstructure. These are for example the parameters of the Bingham distribution itself, which are scaling and concentration parameters, characterizing the size and shape of the underlying fiber bundles. In addition we use additional parameters such as the bundle specific fiber density, the fiber spread and a complexity measure, which reflects the fiber populations present within each voxel and their relative sizes. This allows us to examine the microstructure in the voxel. In this line, the methods presented here offer a novel approach to extend the information on the fODF which can be extracted and incorporated into the analysis beyond the mainly used quantities (fODF peak length and direction). This has been the goal of several recent works (Kaden et al., 2007, Seunarine et al., 2007, Zhang et al., 2007, Sotiropoulos et al., 2012, Dell'Acqua 2013). In contrast to these no new local model is introduced, but we rather focus on extracting information from the widely used constrained spherical deconvolution (CSD).

In summary, the goal of this work is to find a robust parameterization of the fODF, which identifies multiple compartments, each representing a relatively coherent fiber bundle described by a set of meaningful parameters, and to interpret these parameters, as far as possible, in terms of microstructural properties, hopefully increasing the specificity of the assertions made from changes in FA. We used constrained spherical deconvolution as local model, because it directly describes the properties of underlying fiber bundles.

# Material and methods

## *Theory*

### *Spherical deconvolution (SD)*

SD (Tournier et al., 2004, Kaden et al., 2007, Tournier et al., 2007, Descoteaux et al., 2009, Dell'Acqua et al., 2010) translates, for each voxel, the direction dependent signal attenuation into an fODF. The idea behind SD is that the measured signal profile can be expressed as convolution of a kernel K and the fODF Ψ.

$$S(\vec{u}) = \Psi(\vec{u}) \otimes K \qquad (1)$$

The inversion of this relationship, referred to as deconvolution, is used to recover an estimate of the fODF. The resulting fODF is an angular-spatial density, that is, for a given direction it represents a fiber density defined with regards to a single voxel, it therefore describes the angular fiber density (AFD).

We used CSD, as introduced by Tournier et al. (2007), applied to the signal attenuation1 to uncover the fODF. This method assumes the response function (deconvolution kernel) corresponds to the diffusion signal attenuation obtained from a z-axis oriented single fiber and its immediate extracellular neighborhood. One of the key challenges of the method is the suitable estimation of the convolution kernel. One way to do this is to use the average signal attenuation of those voxels within the corpus callosum with an FA above a certain threshold (Tournier et al., 2004), thereby trying to obtain a signal generated by the most coherent fiber arrangements available. Since the deconvolution kernel has to be rotationally symmetric, instead of using the measured signal directly for kernel estimation, we computed the diffusion tensors in the kernel voxels and averaged their principal and their minor (i.e., 2nd and 3rd) eigenvalues. The diffusion tensor was used since it describes the diffusion signal generated by a single fiber population fairly well. If we deconvolve the diffusion signal from a particular voxel with a kernel that has been scaled with an appropriate factor, the resulting fODF represents (an estimate of) the biological angular fiber density in the respective voxel to the extent to which the fibers in that voxel are similar to the average kernel voxel fiber. To scale the signal attenuation for a single fiber, one has to divide the kernel signal attenuation by the corresponding voxel fiber density, which can be estimated from histological work, for example by Aboitiz et al. (1992).

The fODF resulting from deconvolution is represented using a SH expansion, which is truncated at a certain point, defining its order (see Appendix A). The truncation

[1] Note that the MRTrix software package applies the CSD to the diffusion weighted signal rather than the signal attenuation. This introduces a weighting of the fODF by the ratio between the $b_0$ (or T2) value in the respective voxel and the average $b_0$ in the kernel area (e.g., corpus callosum). Hence, the results must be corrected by a factor $b_0$(kernel)/$b_0$(voxel).

introduces ringing phenomena causing so-called negative lobes. The used deconvolution method (CSD) iteratively imposes a non-negativity constraint for a set of control points. This constraint reduces, but not completely eliminates the occurrence of negative lobes in the resulting spherical harmonics representation of the fODF.

Apart from the first spherical harmonic coefficient $c_1$ (see Appendix A, B), there is no straightforward interpretation of the remaining spherical harmonic coefficients in terms of meaningful microstructural properties of the fiber populations. Hence we investigated an alternative parameterization of the fODF. Our general approach is rooted in the observation that the fODF very often comprises several sharp peaks, which are usually interpreted as reflecting relatively collinear fiber populations or bundles. Accordingly, we propose a scheme based on the independent fit of a distinct fiber bundle, approximated by a scaled Bingham distribution, to each peak of the fODF.

## *The Bingham fit*

Fitting Bingham distributions to the peaks of the fODF was first proposed by Seunarine et al. (2007) for the purpose of probabilistic tractography. This was done by calculating the Hessian at the fODF peak of interest and estimating the Bingham parameters from a pre-computed lookup-table.

The Bingham distribution is an analogue to the general bivariate normal distribution on the unit sphere, when concerned with axial data. It is antipodally symmetric, just like the spherical harmonic representation of the fODF. It can be characterized by its density function:

$$b(\vec{u}) = \frac{1}{F_{k_1 k_2}} \exp(-k_1(\overrightarrow{\mu_1}\,\vec{u})^2 - k_2(\overrightarrow{\mu_2}\,\vec{u})^2), \qquad (2)$$

where $\vec{u}$ is a point on the surface of the unit sphere. The normalization constant $F_{k_1 k_2}$ is the confluent hyper-geometric function of matrix argument. The parameters $k_1$ and $k_2$ ($k_2 \geq k_1$) are called concentration parameters and are defined along the axis $\overrightarrow{\mu_1}$ and $\overrightarrow{\mu_2}$. They characterize the width and ovality of the distribution. The larger a concentration parameter gets, the sharper the peak becomes in the direction of the corresponding axis. The direction of the distributions mean $\vec{\mu}_0$ is the axis, that is orthogonal to $\overrightarrow{\mu_1}$ and $\overrightarrow{\mu_2}$ ($\overrightarrow{\mu_0} = \overrightarrow{\mu_1} \times \overrightarrow{\mu_2}$). Because the Bingham distribution and the fODF peaks are not scaled to fit, a parameter s is introduced which together with $F_k$ gives the scaling parameter $f_0 = \frac{s}{F_k} = b(\mu_0)$. Thus, the scaled Bingham distribution, which from here on is referred to as Bingham function, is defined as:

$$\beta(\vec{u}) = s \cdot b(\vec{u}), \qquad (3)$$

For fitting an fODF peak with a Bingham function the five parameters $f_0$, $\overrightarrow{\mu_1}$, $\overrightarrow{\mu_2}$, $k_1$ and $k_2$ need to be estimated. The main orientation is taken to coincide with the direction of the respective fODF peak. The parameter $f_0$ therefore corresponds to the maximum

angular fiber density (AFDmax). In order to estimate the peaks of the fODF, we overlay it with a discrete search grid (in this work we used a grid with 10,242 nodes, corresponding to an angular resolution of 2°). On this grid we estimate points considered close to the local maxima by comparing them to their neighbors. We fit a Bingham function to each of the three largest maxima, ignoring maxima smaller than a certain threshold and consider these further peaks to be noise or ringing artifacts. This does, however, not affect the parameterization as each peak is parameterized separately. In other words, fitting additional peaks does in no way change the results calculated for fitting the other peaks. Therefore, the number of peaks quantified is a parameter depending on the question one is currently investigating. The directions of the selected peaks are fitted by using the respective fODF maximum and a number of surrounding points (neighborhood). For this we compute an orientation matrix (Onstott, 1980, Tanaka, 1999) for each peak. Assuming $\vec{p}_i = (x_i, y_i, z_i), i = 1 \dots N$, to be points near the maximum and $v_i = \Psi(\vec{p_i})$ to be the corresponding fODF value, then the orientation matrix has the following shape:

$$T = \frac{1}{\sum v_i}\begin{bmatrix} \sum x_i^2 v_i & \sum x_i y_i v_i & \sum x_i z_i v_i \\ \sum x_i y_i v_i & \sum y_i^2 v_i & \sum y_i z_i v_i \\ \sum x_i z_i v_i & \sum y_i z_i v_i & \sum z_i^2 v_i \end{bmatrix} \quad (4)$$

This orientation matrix can be understood as a peak fiber tensor, representing the corresponding lobe of the fODF, it however is not directly related to the diffusion tensor, as it represents fibers and not diffusion. The eigenvectors of T correspond to the principal directions of the fODF peak and therefore to the Bingham function fulfilling the maximum likelihood estimate for the points used $\vec{p}_i = (x_i, y_i, z_i), i = 1 \dots N$. This allows estimation of $\overrightarrow{\mu_0}$, $\overrightarrow{\mu_1}$ and $\overrightarrow{\mu_2}$ from the eigenvalue decomposition of T. Because the resulting vectors are biased towards the grid points used, the direction vectors are further improved by gradient ascent optimization.

Using the estimated directions $\overrightarrow{\mu_1}$ and $\overrightarrow{\mu_2}$ in relation to the N neighborhood points $\vec{p}_i$, we are able to obtain a simple system of linear equations, by defining the vector $\beta = \log\left(\frac{b(\vec{p}_i)}{f_0}\right)$ and the matrix A with entries $A_i = [(\vec{p}_i\,\vec{\mu}_1)^2, (\vec{p}_i\,\vec{\mu}_2)^2]_i$. The parameters $k_1$ and $k_2$ can then easily be estimated by solving:

$$\vec{\beta} = A\begin{pmatrix} k_1 \\ k_2 \end{pmatrix} \quad (5)$$

Since the whole method depends on the neighborhood used for representing the peak's properties of interest, one has to ensure that it captures the geometry of the respective fiber peak as accurately as possible, that is to say that all the points belong to the same peak. This is done by successively adding points to the neighborhood under the condition, that the slope of the fODF in this grid point does not change its sign. Due to the fact that points closer to the maximum can be expected to be less biased by the influence of neighboring peaks we additionally only considered neighbors of first,

second and third degree, which on our grid leads to a neighborhood of about 35 points at a maximal angle of 6° to the peak's maximum direction. We performed calculations on the influence of the neighborhood and found nearly no differences in the metrics as long as using a sufficiently large neighborhood, which captures the features of the peak while not including two neighborhood peaks. The fitting scheme is shown in Figure 1.

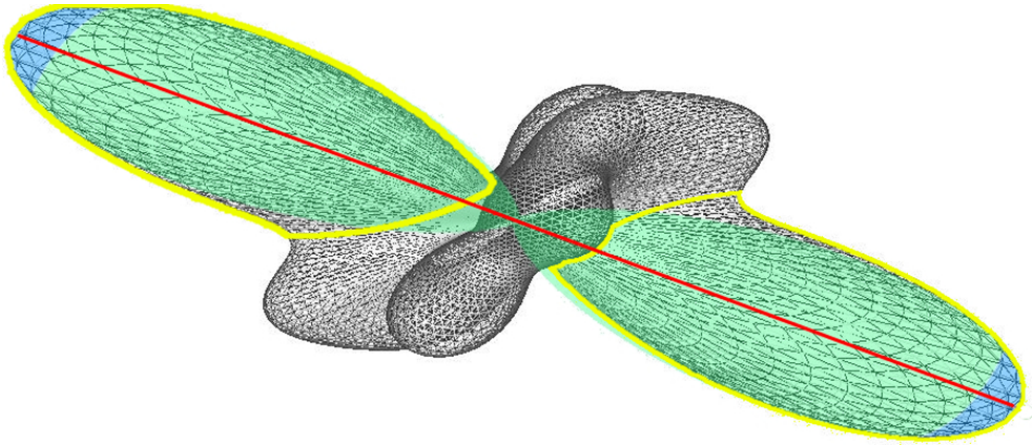

Figure 1: The Bingham fit. The fODF is shown in light grey. The Bingham distribution is shown in green. The maximum direction $\overrightarrow{\mu_0}$ of its largest peak is visualized as the red line. The directions of the Bingham distribution are fitted using a small neighborhood of the maximum direction. The points considered part of the peak are those within the yellow line. To ensure that the neighboring peaks do not have too large an impact, only the neighbors of first, second and third degree are considered, which corresponds to the points in the blue area.

## *Metrics*

Since the Bingham functions represent geometric properties of the fODF peaks and therefore of fiber bundles, the extracted metrics are closely related to the microstructure. Furthermore, since the Bingham function describes the peaks of the fODF, metrics cannot only be computed for each of the bundles separately, but also allow for comparing bundles within a voxel. In the following we will give a short overview of the metrics we investigated.

### *Bingham function parameters*

The metrics most directly estimated are the parameters of the Bingham function themselves. These are the scaling parameter $f_0$ (unit: $\left(\frac{1}{\mathrm{mm^3 rad}}\right)$), the unit-less concentration parameters $k_1$, $k_2$ and the directions $\overrightarrow{\mu_0}$, $\overrightarrow{\mu_1}$ and $\overrightarrow{\mu_2}$. The scaling parameter corresponds to the angular density of fibers, which are aligned with the peak's main

direction. We therefore named this parameter the maximum angular fiber density2 (AFDmax). It has the same unit as the fODF $\left(\frac{1}{\mathrm{mm}^3\mathrm{rad}}\right)$. The two concentration parameters characterize the peak anisotropy and provide a measure for the spread of fiber orientations within one bundle. Large concentration parameters stand for a sharp peak. Further information can be gained from their relation. If the concentration parameters are very different from one another, the peak's cross section is very oval, indicating fan-like spreading, as expected in thin sheet-like fiber populations. In order to make the concentration parameters more accessible to intuition we translated them to peak opening angles ($\kappa_1, \kappa_2$; for more information see Appendix C). These are calculated in a similar manner as the dispersion angles introduced in the work of Sotiropolous et al. (2012) or the orientation dispersion metric defined in the work of Zhang et al. (2012). The difference lies in regarding them individually rather than calculating the mean of the two angles. In the following we will use both descriptions of the concentration parameter. It should, however, always be clear from the context if we are referring to the opening angle or the actual concentration parameter. The Bingham function's directions were not used for quantitative evaluations.

### *Fiber density (FD)*

Another important quantity is the integral of the Bingham function over the sphere. Since the fODF is a measure of the angular fiber density, integration over the sphere yields the fiber density within the bundle. We used numeric integration to solve the integral:

$$\mathrm{FD} = \int_{S^2} \beta(\theta, \phi) \sin\theta \, \mathrm{d}\theta \mathrm{d}\phi. \tag{6}$$

The resulting value is the bundle's fiber density (FD). Since the unit of the AFD is $\frac{1}{\mathrm{mm}^3\mathrm{rad}}$ the fiber density is measured in the unit $\frac{1}{\mathrm{mm}^3}$.

### *Fiber spread (FS)*

The concentration parameters of the Bingham function quantify the colinearity or, vice versa, the spread of the respective bundle. It is, however, desirable to be able to characterize the spread of the whole peak in terms of a single scalar value. This can be done by using the metrics AFDmax and FD to define a new metric:

[2] It should be noted that in the work of Raffelt et al. (2012b), this parameter is characterized as the apparent fiber density. The quantity described however is actually the angular fiber density within the peak's maximum direction, which for sufficiently high b-values is closely related to the apparent fiber density. In essence, a different parameter is measured at the b-values normally used, we therefore call this quantity the $\mathrm{AFD}_{\mathrm{max}}$.

$$\mathrm{FS} = \frac{\mathrm{FD}}{\mathrm{AFD}_{\max}}. \tag{7}$$

This metric compares maximum AFD to average AFD. The wider the peak is, the closer the maximal and average angular fiber densities are within one bundle, which leads to a higher value of FS. When there is a wide peak the average and maximum value are closer than when there is a sharp peak. The unit of the FS is radians. It should be noted that the value of the metric FS is equal to the value of the normalization constant of the non-scaled Bingham distribution, in other words the connection to the concentration parameters is given by the integral over the exponential of the Bingham distribution.

## *Complexity (CX)*

As mentioned above, the ability to distinguish the presence of separate fiber bundles in a voxel allows us to construct metrics to compare the bundle's properties Comparing the FD of different bundles within a voxel leads to a new metric called (structural) complexity (CX). This metric's value increases when the fiber structure becomes more complex and fewer of the fibers in the voxel are contained in the largest bundle alone. We define FDi to be the fiber density of the i-th largest peak of the fODF, then CX is defined by:

$$\mathrm{CX} = \frac{n}{n-1}\left(1 - \frac{\max_{\mathrm{i}} \mathrm{FD_i}}{\sum_{i=1}^{n} FD_i}\right), with\ n > 1.. \tag{8}$$

The value is scaled to lie between 0 and 1. If a single fiber is present within a voxel the CX is zero. The CX becomes equal to one when all peaks in the voxel have the same fiber density.

Exemplarily four fiber configurations and the respective metrics derived from the Bingham function as well as the FA are presented in Figure 2.

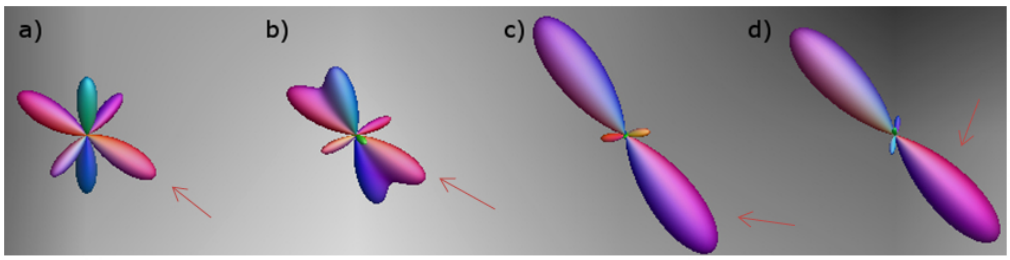


| Metric | a) | b) | c) | d) |
|---|---|---|---|---|
| $k_{11}$ | 14.83° | 23.40° | 16.12° | 16.09° |
| $k_{21}$ | 14.12° | 14.98° | 15.70° | 14.87° |
| $AFD_{max1}$ | $1.77\frac{1}{mm^3 rad}$ | $1.63\frac{1}{mm^3 rad}$ | $3.35\frac{1}{mm^3 rad}$ | $3.64\frac{1}{mm^3 rad}$ |
| $FD_1$ | $0.67\frac{1}{mm^3}$ | $1.19\frac{1}{mm^3}$ | $1.69\frac{1}{mm^3}$ | $1.75\frac{1}{mm^3}$ |
| $FS_1$ | 48.13° | 41.82° | 28.65° | 26.93° |
| CX | 0.54 | 0.79 | 0.21 | 0.17 |
| FA | 0.31 | 0.37 | 0.54 | 0.61 |

Figure 2: Four fiber configurations and the metrics related to the largest peak in each of these fiber configurations. The glyphs were calculated with MRtrix. The data is part of the dataset discussed in section 3.3. The indices of the metrics indicate the values are related to the first, i.e. largest peak. For easier reference the peak is indicated by a red arrow in each of the fiber configurations. It should be noted that both the side indicated by the arrow as well as the antipodal symmetric other half are understood as one peak.

## *Evaluation*

For evaluation, we applied our methods to three types of data: computer simulated data, measured data from a physical phantom, and human brain data.

The simulated data were generated in such a way that the underlying fiber distributions were exactly covered by the model (i.e., Bingham functions) and the ground truth was known. This was achieved by Bingham distributing the fiber orientation, and then convolving that distribution by the diffusion tensor, which was taken to represent the diffusion profile of a single fiber population. As the Bingham distribution represents a Gaussian in spherical coordinates, its use here is not only convenient, but a natural choice, at least if one assumes random deviations from a main fiber direction. For these Bingham distributions we randomly varied the parameters and then correlated the reconstructed values with the ground truth. The diffusion signal was calculated by computing the forward model, that is, convolution. We did this for a single bundle as well as for a configuration involving two bundles that cross at a random angle. We assumed the signal attenuation generated by a single fiber, that is the deconvolution

kernel, to be appropriately described by a diffusion tensor with an FA of 0.86 and the eigenvalues $\lambda_1 = 0.0014\ \mathrm{mm}^2/\mathrm{s}$ and $\lambda_2 = \lambda_3 = 0.000177\ \mathrm{mm}^2/\mathrm{s}$, which corresponds to a mean diffusivity (MD) of $0.0006\ \mathrm{mm}^2/\mathrm{s}$. This kernel was estimated from the corpus callosum voxels of a human dMRI data set. The parameters of the Bingham distributions were chosen to be uniformly distributed within intervals estimated from real data, so $0° < \kappa_1, \kappa_2 < 90°$; $0 < f_0 < 3$ in the single fiber case. For the crossing case we assumed two Bingham distributions, crossing at an arbitrary angle between 60° and 90° and reduced the parameter space ($15° < \kappa_1, \kappa_2 < 30°$; $1 < f_0 < 2$) to ensure that crossing are properly resolved and to minimize Bingham function overlapping. We performed sixth and eighth order constrained spherical deconvolution on these datasets. Afterwards we calculated the correlation between the reconstructed values of the metrics and the ground truth. Finally, we analyzed the influence of noise on the results in order to determine the robustness of the Bingham fit method. This was done by adding a varying simulated Rician noise (Aja-Fernandez et al., 2008) to the simulated diffusion signal calculating the fODF and then applying the Bingham fit. The kernel used for deconvolution was left unchanged, since in practice it is calculated over a large number of voxels, reducing the influence of the noise.

To test the Bingham fit and to estimate how it behaves in more intricate geometries and under more realistic conditions, while still having ground truth knowledge to validate the results, we used the phantom data from the Fiber Cup contest (Fillard et al., 2011). The creation of the physical phantom is described in the work of Poupon et al. (2008). The dataset we used was measured at a b-value of 2000 and with a spatial resolution of 3 mm. A kernel represented by a diffusion tensor with major eigenvalue $\lambda_1 = 0.0018\ \mathrm{mm}^2/\mathrm{s}$ and minor eigenvalues $\lambda_2 = \lambda_3 = 0.0014\ \mathrm{mm}^2/\mathrm{s}$ was used. This tensor has an FA of 0.12, which is the average FA in the single fiber areas of the physical phantom. This FA value, which is much lower than in a human dataset, can be explained by the difference in diffusion properties of water in synthetic and biological fiber bundles. It does not stem from additional crossings, as the fiber configuration is known over the entire phantom, but it rather represents a qualitative difference in the signal of the synthetic fibers.

Finally, we applied our methods to in vivo human diffusion data. The experimental setup was approved by the local ethics committee of the University of Leipzig and the participant gave written informed consent before being included in the experiment. We acquired a 3D T1 weighted structural MPRAGE scan (spatial resolution = 1 $\mathrm{mm}^3$) and a high resolution dMRI scan from a young right-handed volunteer on a whole-body 3 Tesla Siemens Tim Trio magnetic resonance scanner (Siemens, Erlangen, Germany) equipped with a 32-channel head array coil. For the dMRI we employed a spin-echo echo planar imaging (EPI) sequence (TE = 85 ms; TR = 13.8 s; 144 x 144 image matrix; FOV = 220 x 220 $\mathrm{mm}^2$; 85 axial slices (no gap); spatial resolution: 1.5 x 1.5 x 1.5 $\mathrm{mm}^3$, GRAPPA acceleration factor 3, no cardiac gating, 60 diffusion directions evenly distributed over the hemisphere, b-value = 1000 s/mm2). Seven images without any diffusion weighting (b0) were obtained: one at the beginning of the scanning sequence and one after each block of 10 diffusion-weighted images as anatomical reference for offline motion

correction. To increase signal-to-noise ratio (SNR), we repeated the measurement three times. The structural scan was reoriented to the sagittal intercommisural plane and the brain was segmented from the skull. The b0 and b1000 images were used to estimate motion correction parameters of the dMRI sequence using the rigid body registration (Jenkinson et al., 2002), implemented in FSL (FMRIB Software Library, University of Oxford, http://www.fmrib.ox.ac.uk/fsl/). We combined the motion correction for the dMRI data with the global registration to the T1 anatomy, corrected the gradient direction for each volume with the rotation parameters, resampled the registered images to an isotropic voxel resolution of 1.5 mm and averaged the three acquisitions. Finally, we computed the diffusion tensor, the three eigenvectors, and the FA value for each voxel. On this dataset we performed an eighth-order SH approximation of the fODF using MRtrix (Tournier et al., 2012; http://www.brain.org.au/software/mrtrix/). After applying CSD to the signal attenuation we normalized the result to the number of fibers in the deconvolution kernel. The kernel FD was estimated as $3.717\ 10^5$ fibers per $mm^3$ in accordance to (Aboitiz et al., 1992). The normalization of the fODF $\Psi$ in each voxel amounts to:

$$\Psi_{\text{norm}} = \Psi \cdot \text{FD}_{\text{Kernel}}. \tag{9}$$

The same normalization was applied to the phantom data using the fiber density of 1900 fibers per $mm^3$, as described by Fillard et al. (2011).

We then calculated the parameters of the Bingham functions. To estimate the maxima of the SH we used a regularly tessellated search grid constructed by 5 iterative refinements of a regular icosahedron resulting in 10,242 vertices and 20,480 faces.

We chose the three largest peaks found on the search grid and approximated the corresponding fODF peaks. In principle, more peaks are possible, depending on the quality and quantity of the available measurement information. The Bingham fit was performed using a neighborhood size of 35 points, that is to say all direct neighbors and neighbors of second and third order, around each maximum, which corresponds to an angle of maximal 6° per direction for determining the parameters of the Bingham function.

## Results

### *Simulated data*

After establishing a method for generating metrics from the approximation of the fODF we established the relation of these metrics to the ground truth. This was done using simulated data. Our main goal here was to derive rules on how to interpret the metrics after having applied our fODF decomposition approach to real data. For this we needed to focus on several questions.

First, we needed to know how well the metrics correlated with the ground truth and how the order of the SH reconstruction as well as the chosen neighborhood and noise affect the correlation. This allowed us to be certain about the range in which the metrics and the ground truth were well connected.

We found that in the single fiber case the reconstructed values correlate to the ground truth very well. This can be seen in the left column of Figure 3. Here the ground truth and the reconstructed data show a correlation $R^2$ very close to 1 for the metrics AFDmax, FD, FS and $\kappa_2$. Merely $\kappa_1$ is correlated slightly worse. Of interest here is the strong bias in both concentration parameters for angles smaller than approximately 15° for the eighth-order SH reconstruction and 17° for the sixth-order. Outside of this area the concentration parameters show perfect alignment with the ground truth values, as do the values observed for the other metrics. Below those angles however, the concentration parameters are reconstructed as nearly constant value independent of their ground truth value. For the SH series of lower order this indicates an inability to fit sharper peaks. Since this fit error has an impact on the other metrics as well, we used only concentration angles larger than 20° for the analysis of the other metrics (AFDmax, FD, FS).

Next we analyzed the crossing fiber model. The results are shown in the middle and right column of Figure 3. As can be seen, the crossing causes interference between the two peaks, which leads to a lower correlation of the reconstructed values to the ground truth than in the single fiber model. The metrics AFDmax, FD and FS are more stable than the concentration parameters, that is, they show a higher correlation to the ground truth.

We also calculated the correlations for the CX metric and the crossing angle. These results are shown in Figure 4. The CX is recovered fairly well, that is to say that it shows high correlation, although the design of the simulation experiment leads to unevenly distributed CX values. The bias in the CX metric stems directly from the bias in the recovered FD values. The crossing angle on the other hand shows a strong bias depending on the order of SH reconstruction.

For further evaluation we mapped the crossing angle dependence of the correlation of the reconstructed values and the ground truth for sixth and eighth-order SD (shown in Figure 5). A noteworthy point is that the reconstructed parameters AFDmax, FS and FD

of the first peak highly correlate with the ground truth (values between 0.75 and 0.90). The values of $\kappa_1$ and $\kappa_2$ show high correlation for an angle above 60° and below 20°. Between 20° and 50° the correlation drops off strongly for these parameters. This drop is connected to the minimal resolution of CSD, in other words, below a crossing angle of 20° the CSD only resolves a single peak. However, as the angle increases a second peak can be observed. This second peak is neither resolved at the correct angle nor at the original size and width, but rather experiences strong cross-talk effects from the other peak, while itself distorting the other peak. At a crossing angle of 50° the two peaks are far enough apart to not influence each other strongly enough anymore. This problem is not specific to the fitting approach we used, but rather is an issue of the underlying CSD model.

For the second peak the correlation is low up to an angle of between 50° and 60°, which is the angle for which the peaks can correctly be separated. Furthermore one can observe that a higher order leads to a better correlation.

Finally we analyzed the influence of noise. The resulting correlation coefficients are shown in Table 1 for the single fiber case and Table 2 for the crossing fiber case. In the single fiber case (Table 1) most of the correlations do not depend strongly on the SNR values we investigated. The exceptions to this are the metrics $\kappa_1$, which shows good correlation only for an SNR of above 20, and FS, which is not well correlated up to a SNR of 40. The influence noise has on the correlation of the reconstructed FS to the ground truth is somewhat greater in case of a higher deconvolution order.

For the crossing fiber case the correlations are more dependent on the SNR. Here many metrics are badly correlated for SNR values of less than 20. Again the parameters $\kappa_{11}$ and $\kappa_{21}$ do not show high correlation. Furthermore the FS for both bundles is not correlated well up to a SNR of 40. Also the CX metric is not correlated well in the presence of noise.

As can be seen from Table 1 and Table 2, the most stable metrics in presence of noise are AFDmax and FD. These two metrics are related to the first statistical moments of the Bingham distribution. The more unstable metrics ($\kappa_1$, $\kappa_2$, FS) are related to the second statistical moments. Interestingly the deconvolution order does not have a particularly profound effect on the correlation in the presence of noise.

The question remains to what extent the deviations in the reconstructed fiber bundles originate from the SH approximation or from the Bingham fit. To investigate this matter, we used the human brain dMRI data and measured, for all voxels, how well the fitted Bingham distributions described the peaks of the corresponding SH approximated fODF peaks. The accuracy of the fit was quantified by calculating the difference between the Bingham function and the fODF within the peak area (Fig. 1). The results are shown in Figure 6. The Bingham functions represent the peaks of the fODF very well. This can be substantiated further by the normalized histogram of the fit difference in percent. In only about 5% of the voxels the difference is larger than 3%.

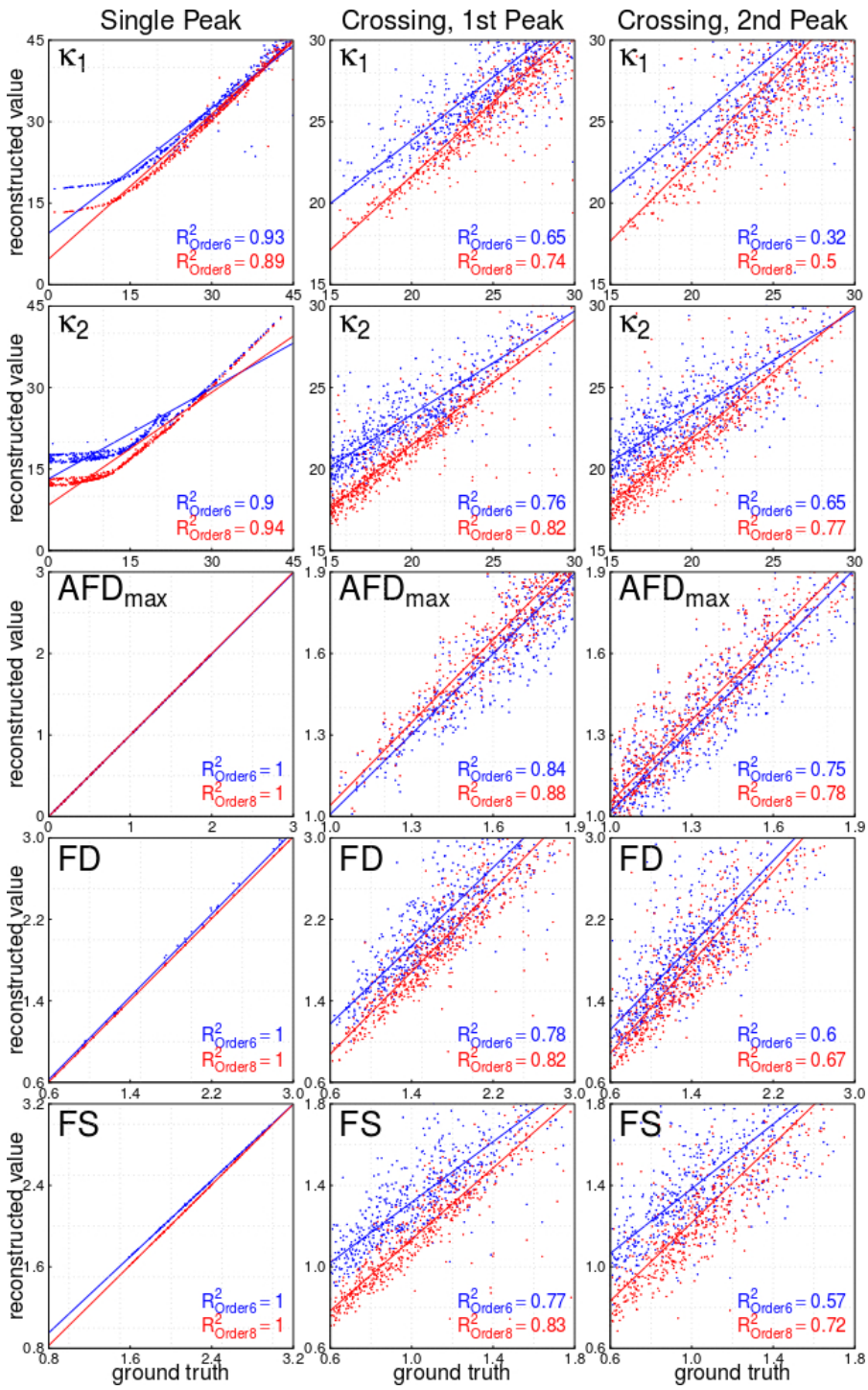


Figure 3: Correlation of ground truth and reconstruction. Here the correlations of metrics calculated are depicted using the Bingham fit and their ground truth values. Ground truth and reconstructed values are shown in the unit of their respective metric. The left column shows metrics reconstructed for a single fiber population as being present within a voxel. The middle and right column show the metrics for the first (middle column) peak and second (right column) peak in the case of fiber crossing. In each of the pannel the reconstructions are plotted for sixth (blue) and eighth (red) order SH series representation of the fODF. The lines show the linear regression results. The corresponding Pearson

coefficients ($R^2$) are displayed on the bottom right of each pannel. As can be seen, the spread of each of the parameters is smaller for the single fiber model, which leads to higher correlations.

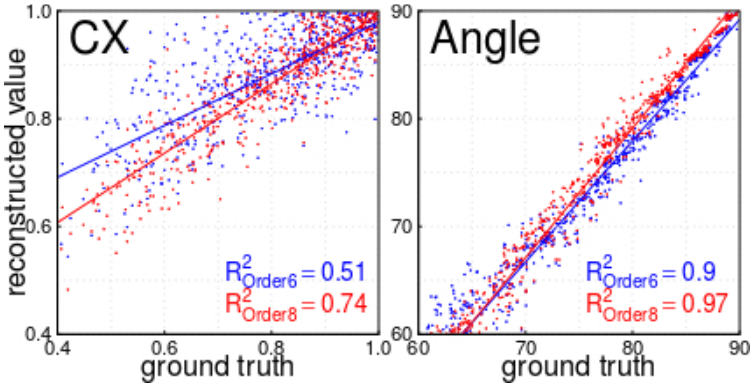


Figure 4: Correlation of CX as well as the crossing angle to the ground truth. Here the correlation for the metric CX as well as for the resolved crossing angle between the two peaks involved in the simulated crossing are shown. Colors and labels are the same as in Figure 3.

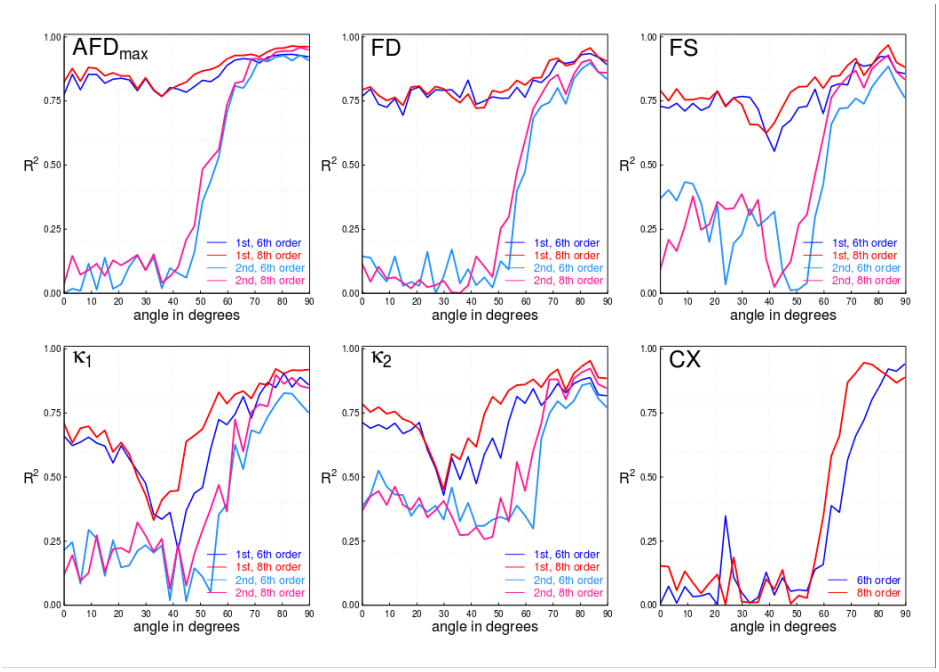


Figure 5: Angular dependence of the metrics ground truth correlation on the fiber crossing angle. These plots show how the correlation between the reconstructed values and the ground truth depends on the fiber crossing angle and the order of spherical harmonic series approximation. While the correlation of the values reconstructed from the largest peak are quite high (between 0.80 and 1.00), except for the area between 10° and 40°, where lower values can be observed for some parameters (FD, FS and especially $\kappa_1$), the parameters of the second peaks do not correlate well with the ground truth until a crossing angle of 50° is reached. Generally the higher order reconstruction shows better correlation with the ground truth.

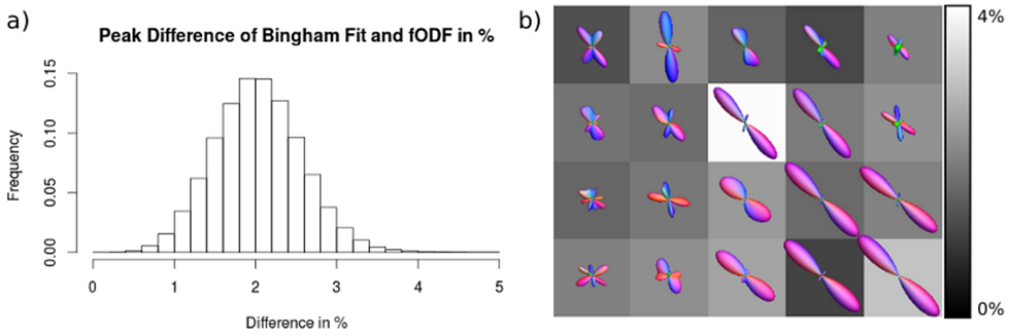


Figure 6: Difference between Bingham fit and fODF. On the left (a) the histogram of the difference between the Bingham fit of the largest three peaks and the fODF is shown for a human brain dataset. The difference was calculated at the nodes of the search grid used for the fitting the Bingham function to the peak and set into relation to the fODF values. On the right (b) the difference is visualized for a selection of voxels. The background color indicates the magnitude of the difference. The fODF is depicted as glyph for comparison.

| Correlation to ground truth in the presence of noise | | | | | | |
|---|---|---|---|---|---|---|
| | SNR | k1 | k2 | AFDmax | FD | FS |
| 6th order | 10 | 0.2 | 0.54 | 0.99 | 0.69 | 0.11 |
| | 20 | 0.49 | 0.73 | 1 | 0.98 | 0.12 |
| | 30 | 0.61 | 0.8 | 1 | 1 | 0.26 |
| | 40 | 0.71 | 0.86 | 1 | 1 | 0.51 |
| | ∞ | 0.95 | 0.9 | 1 | 1 | 1 |
| 8th order | 10 | 0.26 | 0.64 | 1 | 0.72 | 0.021 |
| | 20 | 0.44 | 0.76 | 1 | 0.98 | 0.13 |
| | 30 | 0.65 | 0.82 | 1 | 1 | 0.18 |
| | 40 | 0.74 | 0.86 | 1 | 1 | 0.32 |
| | ∞ | 0.94 | 0.94 | 1 | 1 | 1 |

Table 1: Correlation of ground truth and metrics for a simulated single fiber configuration, derived from the fODF Bingham fit for different SNR. The first column contains the SH order used for deconvolution. The second column contains the SNR used in the simulation. The remaining columns contain the correlation to the ground truth for metrics derived from the Bingham function as described in chapter 2.2. These are in order the concentration parameters k1 and k2, the maximum angular fiber density (AFDmax), the fiber density FD and the fiber spread FS.

| Correlation to ground truth in the presence of noise | | | | | | | | | | | | | |
|---|---|---|---|---|---|---|---|---|---|---|---|---|---|
| | **SNR** | **$k_{11}$** | **$k_{12}$** | **$AFD_{max}1$** | **$FD_1$** | **$FS_1$** | **$k_{21}$** | **$k_{22}$** | **$AFD_{max}2$** | **$FD_2$** | **$FS_2$** | **CX** | **angle** |
| 6th order | 10 | 0.058 | 0.21 | 0.6 | 0.41 | 0.15 | 0.046 | 0.1 | 0.28 | 0.24 | 0.11 | 0.039 | 0.42 |
| | 20 | 0.18 | 0.51 | 0.77 | 0.6 | 0.43 | 0.15 | 0.39 | 0.47 | 0.32 | 0.3 | 0.12 | 0.83 |
| | 30 | 0.26 | 0.61 | 0.8 | 0.61 | 0.48 | 0.17 | 0.45 | 0.46 | 0.32 | 0.38 | 0.27 | 0.87 |
| | 40 | 0.39 | 0.66 | 0.8 | 0.7 | 0.59 | 0.24 | 0.57 | 0.48 | 0.4 | 0.49 | 0.26 | 0.89 |
| | ∞ | 0.61 | 0.73 | 0.83 | 0.74 | 0.72 | 0.35 | 0.59 | 0.71 | 0.55 | 0.54 | 0.47 | 0.95 |
| 8th order | 10 | 0.029 | 0.19 | 0.56 | 0.34 | 0.11 | 0.054 | 0.13 | 0.44 | 0.28 | 0.12 | 0.13 | 0.38 |
| | 20 | 0.18 | 0.51 | 0.79 | 0.57 | 0.44 | 0.15 | 0.38 | 0.52 | 0.33 | 0.32 | 0.16 | 0.59 |
| | 30 | 0.28 | 0.66 | 0.84 | 0.61 | 0.52 | 0.22 | 0.5 | 0.49 | 0.41 | 0.46 | 0.39 | 0.8 |
| | 40 | 0.36 | 0.68 | 0.85 | 0.68 | 0.62 | 0.28 | 0.58 | 0.51 | 0.42 | 0.51 | 0.36 | 0.81 |
| | ∞ | 0.64 | 0.78 | 0.88 | 0.77 | 0.77 | 0.43 | 0.76 | 0.84 | 0.64 | 0.69 | 0.76 | 0.97 |

Table 2: Correlation of ground truth and metrics for a simulated fiber crossing configuration, derived from the fODF Bingham fit for different SNR. The first column contains the SH order used for deconvolution. As in table 1, the second column contains the SNR used in for the simulation. The further columns contain the correlation to the ground truth for the parameters of the Bingham function fit for the two largest peaks, as described in chapter 2.2. Besides the metrics mentioned in Table 1, the correlation is shown for the complexity CX and the crossing angle.

## *Phantom data*

To evaluate the metrics in a more meaningful, albeit somewhat less controlled setting, we applied our decomposition method to phantom data. Here we were especially interested in finding out if the metrics would be able to uncover the underlying fiber structure from the data. We focused on the metrics AFDmax, FD, FS and CX, as well as the FA for comparison. The goal was to check what extra information could be revealed from the Bingham function based metrics in a controlled environment. The results are shown in Figure 7. The color maps in each example were scaled to maximize the contrast in the images. Values larger than the maximum value were set to red, while values smaller than the minimum were set to dark blue.

It should be noted that due to the diffusion properties of the synthetic phantom, the FA values are generally much lower than in biological tissue. However, this change in diffusion properties does not influence the values derived from the fODF because they are captured by the diffusion kernel.

We will begin by focusing on comparing the FA and the CX. Since we know the actual fiber configurations for the phantom, shown in panel a) of Figure 7, we can validate our structural complexity metric by applying it to these configurations and compare it to the FA. While the complexity measure is mostly inversely proportional to the FA, in the area marked as A and circled in red, the complexity further specifies the information gained from FA. In this area the complexity is high, which indicates a crossing fiber configuration. The value of 0.5 for the complexity metric (using a peak number of n = 3) indicates a crossing of one large bundle containing approximately 2 times the number of fibers as the smaller bundles combined. The FA in the circled area is rather high despite the crossing, since the smaller bundles do not influence the tensor as strongly as the larger one. When following the two crossing bundles separately one can derive the information for the voxel from the local surroundings. The complexity measure thereby not only increases the specificity, but in this case uncovers more microstructural information than the FA by indicating the underlying structure without the need to evaluate the surrounding structure. Similar information can be gained from the comparison of the AFDmax and FD for the different peak sizes. The AFDmax and the FD of the first peak show a very similar qualitative behavior to the FA. The further structural information can almost completely be gathered from the second and third peak. It should be noted that the CX is high in most of the top half of the phantom, especially close to the border. This is might be caused by a lower SNR in these branches which also present lower FA values. Another possible reason might lie in the possible inhomogeneity in the underlying fiber density, due to the construction of the phantom.

Intrinsic properties stemming from the construction of the phantom data are uncovered by the metric FS. For the major fiber bundles this metric is close to constant over the whole phantom, except for some noise voxels. This indicates that no significant fanning is present in this phantom and shows that the bundles are almost all configured the same way. This leads in particular, to AFDmax and FD being very similar, since they are then related by a constant factor. One aspect of the phantom dataset is that the background is very noisy, which leads to a strong influence on voxels in the boundary regions of the synthetic fiber populations. This influence is shown by the metric CX, which indicates a sharp increase in complexity in the vicinity of the fiber bundle boundaries.

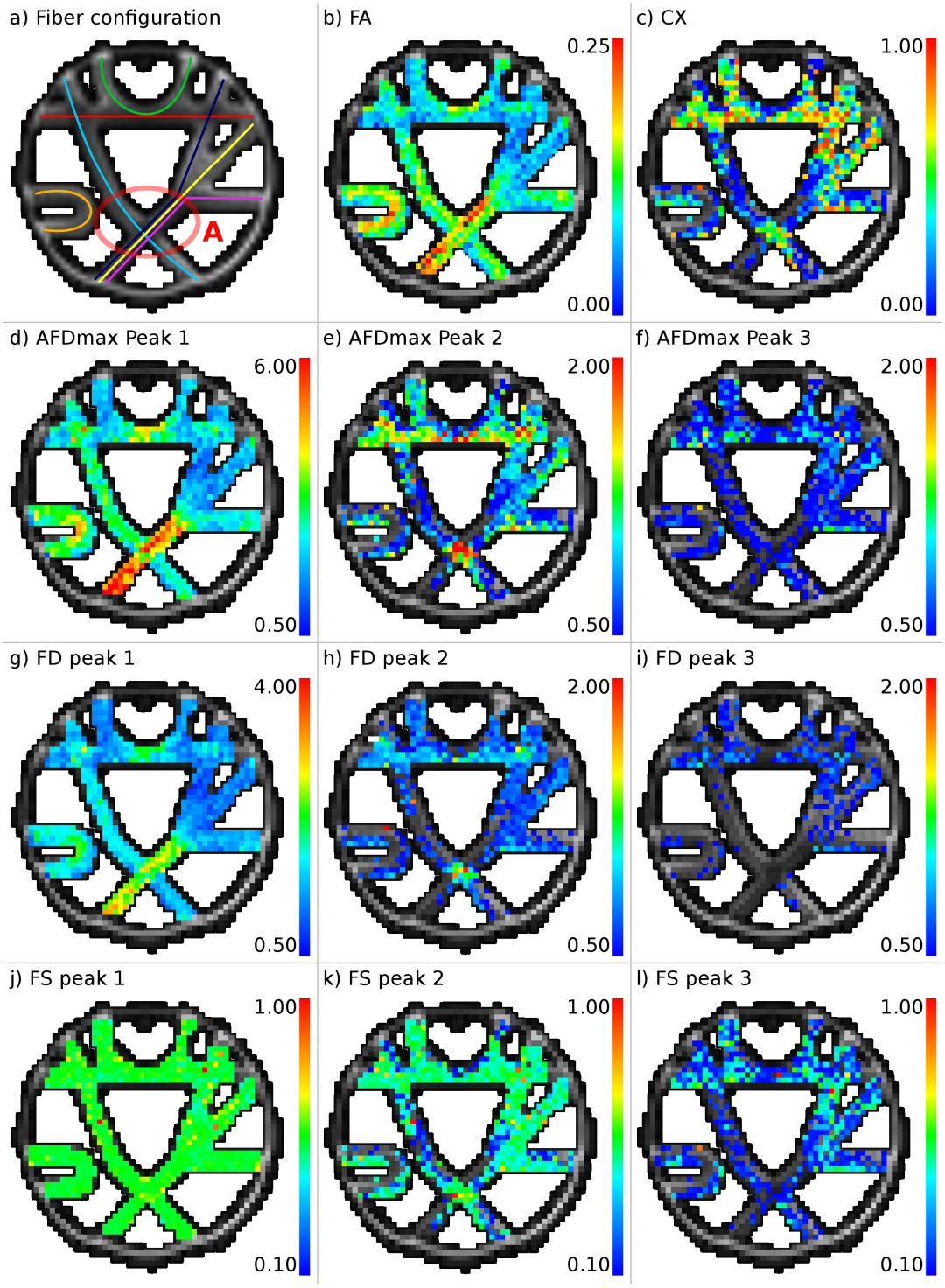


Figure 7: Metrics from phantom data. Here the metrics calculated from the phantom data are mapped upon the b0 image. Color maps were optimized for contrast. Values above the maximum value are set to red, ones below are set to zero. Zero values are not shown. The geometry is depicted in panel a). The metrics are shown in panels b) through l).

## *Human data*

Next we applied the Bingham fit to fODFs from in-vivo MRI data of a human brain and evaluated the derived metrics. To increase the visual effect of these metrics we applied a smoothing with a gauss kernel of 1 mm. The original maps are shown in Figure D.1 and D.2 in Appendix D. The smoothened results are depicted in Figure 8. Again the FA and the AFDmax as well as the FD of the first peak appear qualitatively similar, with high values in the corpus callosum (CC) and the corticospinal tract (CST) and low values in crossing areas and in the vicinity of the cortex (correlations as shown in Figure 10: FA to AFDmax and FA to FD both 0.62). The CX metric appears to be negatively correlated to these metrics (-0.57). One is clearly able to distinguish the crossing areas from areas with aligned fiber structure from the CX map. In other words this metric has higher values in the crossing regions, while CC and CST are shown to have medium to low structural complexity. The fiber spread also shows the expected behavior for the first peak by being higher in the corona radiate and other fanning white matter regions, while being lower and close to constant in the other regions. FS is especially high in the white matter close to the cortex.

The metrics derived from the Bingham functions fitting the secondary and tertiary peaks of the fODF are shown in Figure 9. As can be seen, the maps for the higher order peaks get more and more sparse due to those peaks not being present in the fODF.

The AFDmax parameter is significantly smaller for the second and third peak, than for the first peak. It is also the parameter by which the peaks are sorted. While the map of this parameter of the first peak was similar to the FA, the parameter for the second and third peak was significantly different. In the CC and CST the AFDmax from the second and third peak is low, while in the crossing regions and at the grey-white-matter boundary it is high.

The FD maps show strong dissimilarity between the first, second and third peak. While the first peak's map is similar to the FA, the second peak's map resembles the CX. The third peak's FD on the other hand is relatively smooth and has significantly smaller values.

Finally the correlations between the metrics are depicted in Figure 10. Here some interesting observations can be made. The FA is negatively correlated to the CX as well as positively correlated the AFDmax and FD of the first peak. It shows little to no correlation to any other metric, especially those of the non-primary peaks. This indicates a strong connection between the FA and the shape of the first peak. The CX on the other hand, is correlated strongly to all metrics, while the AFDmax and FD are mainly correlated within corresponding peaks, showing little to no inter-peak relationship.

To infer the spatial connection between the metrics AFDmax, FD, FS, CX and the FA, we visualized the spatial distribution of the summands of the Pearson correlation coefficient ($R^2$) in Figure 11. The average of all the summands gives the correlation between the FA and the metric, as depicted in Figure 10. Here one can observe that the

FA and the metrics AFDmax, FD and CX are strongly connected in areas without a high number of fiber crossings. The FS shows only a low correlation overall and also the spatial map does not reveal any areas of high connection, except for small positive summands in the crossing areas and negative values in the areas without strong crossings.

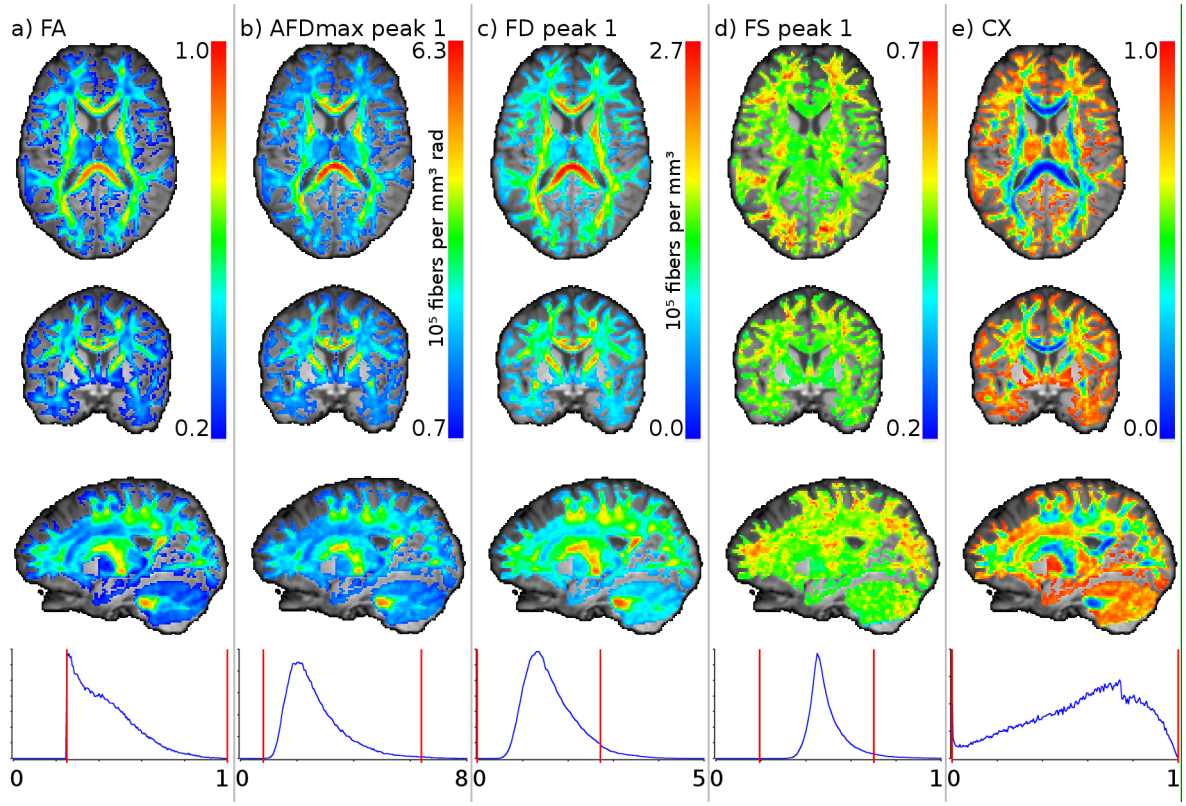


Figure 8: Primary metrics mapped on the human brain. Displayed here are the smoothed maps of the metrics FA, CX as well as the three metrics AFDmax, FD and FS, which characterize the first peak. The images of the metrics were masked to the white matter using an FA map with a threshold of 0.15, which were manually expanded to cover the white matter and the thalamus. These maps were then overlaid on an interpolated T1 image and scaled for contrast. The boundaries for the scaling are marked in the histograms at the bottom. The y axis in the histogram represents the number of voxels in which a certain value occurs. These are the images obtained from smoothing the original metrics before applying the white matter mask. The results without the smoothing steps can be found in Appendix D (Figure 13).

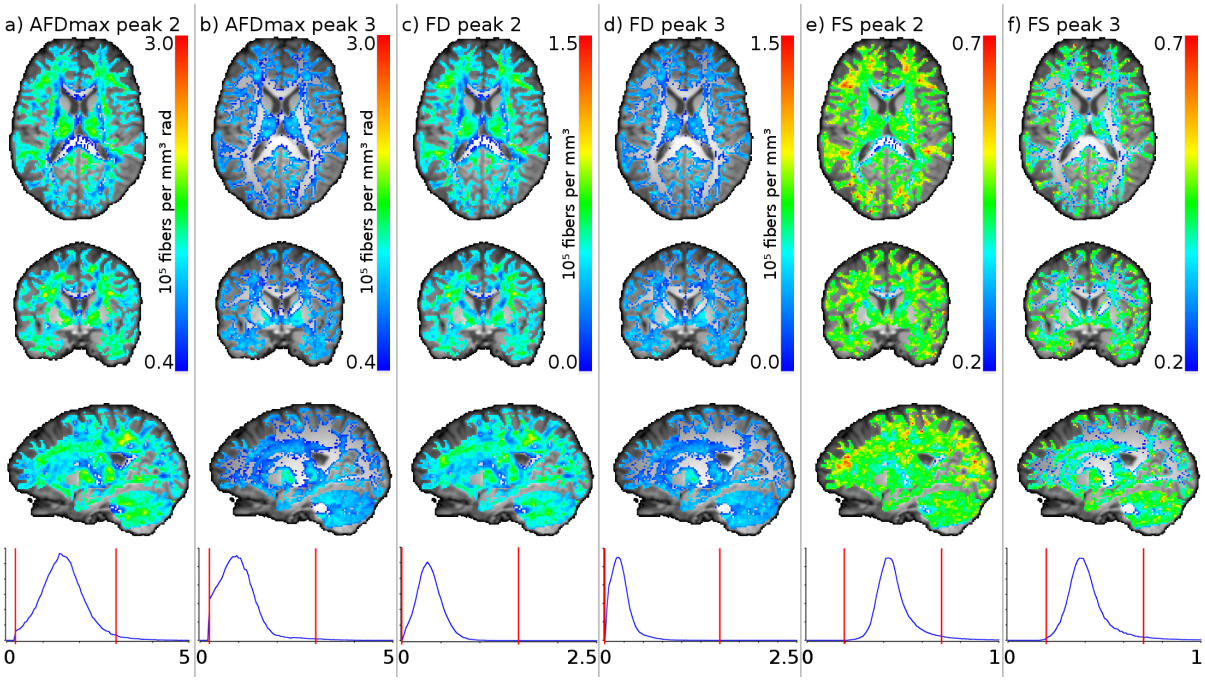


Figure 9: Metrics of secondary and tertiare fODF peaks. These maps were created as those in Figure 8, including the scaling and the histograms at the bottom. The maps for the non-interpolated metrics can be found in Appendix C (Figure 14).

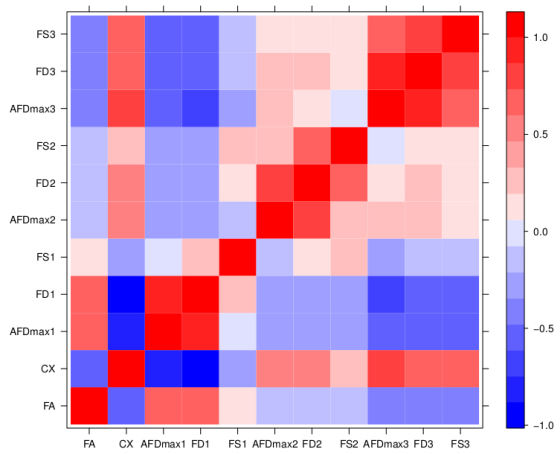


Figure 10: Correlation between metrics. This image shows the correlation structure of the metrics. For correlation purposes a white matter skeleton was used to map the metrics. All voxels for which either of the metrics was equal to zero were dismissed. As can be seen, 3 clusters can easily be identified. The first contains FA, CX, AFDmax1, FD1, the second AFDmax2, FD2 and FS2, the third AFDmax3, FD3 and FS3. This indicates a strong connection between FA, as well as the shape of the first peak and the microstructural properties at the same time.

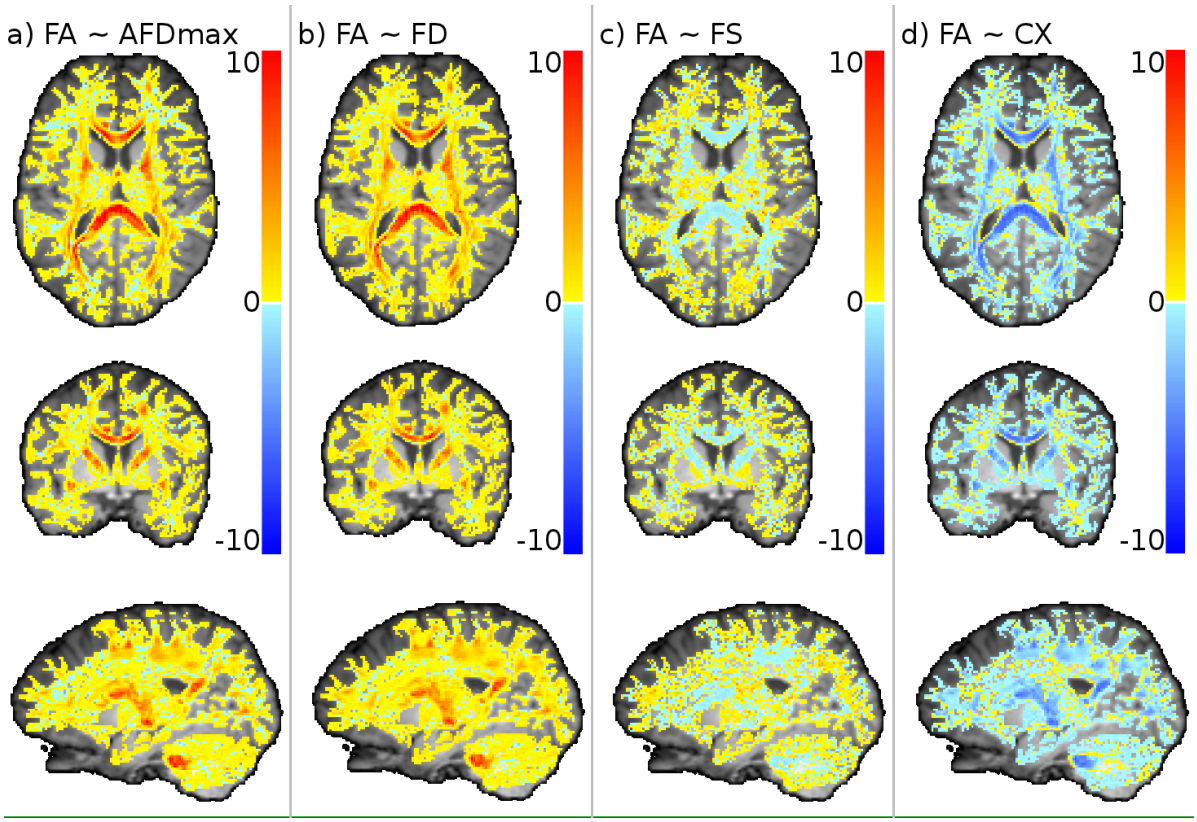


Figure 11: Spatial mapping of contribution to correlation with FA. The values correspond to the summands of the Pearson correlation coefficient. The average of these values over the whole masked region gives the correlation, which is shown in Figure 10. As can be seen, for AFDmax, FD and CX high values (as with CX) low values can be found in the main fiber bundles, i.e. especially in regions without major crossings. The FS shows small negative values mainly in areas without fiber crossings.

## Discussion

We used Bingham functions, that is, scaled Bingham distributions, to characterize the peaks of the fODF estimated from constrained spherical deconvolution (CSD). The motivation for choosing such an approach lies within the observation that CSD and the corresponding fODF are widely used tools for the analysis of diffusion data that are easy to apply and do not require a priori model choices. It therefore is of interest to find a parameterization, which allows for increasing the information which can be gained from the results of CSD. Furthermore this approach can be applied to every method which gives an ODF. The only difference then lies in the interpretation of the derived metrics.

The fODF information which has so far been used in analysis mainly includes the length of the (largest) peaks and their direction. We presented a novel approach for extracting more in depth metrics on the fODF, which can be quantitatively evaluated. This is in line

with several recent works (Kaden et al., 2007, Seunarine et al., 2007, Zhang et al., 2012, Sotiropoulos et al., 2012, Dell'Acqua et al., 2013). In our approach we assumed the peaks of the fODF to reflect the microstructural fiber bundles present in a voxel. The fitted Bingham functions share geometric properties with the fODF, which can directly be translated to metrics describing properties of the underlying fiber bundle. The introduced metrics were the fiber density (FD), maximum angular fiber density (AFDmax), the fiber spread (FS) and the structural complexity (CX). We validated our metrics using simulations and then investigated their behavior using a physical phantom. Here, the known fiber layout enabled us to investigate how our metrics compared to the FA and show areas where they increase its specificity. Finally we applied our methods to in-vivo brain scans. We demonstrated how the proposed metrics can be used on their own to draw conclusions on the underlying microstructure, and how they may help to provide findings from the FA with additional meaning, thus increasing specificity.

In detail we found that, as expected, the AFDmax specifies areas of high fiber colinearity, the FD gives insights into the fiber density, and the CX correctly identifies regions of fiber crossings. Furthermore, we found that the CX anti-correlates to the FA, while the AFDmax as well as the FD of the largest peak strongly correlate to the FA (as shown in Figure 10). Besides this, we showed that the correlation mainly originates from areas without major fiber crossings (Figure 11), therefore these metrics can be believed to hold information additional to that of the FA. This confirms that the FA is a metric describing a mixture of properties, which can be specified using the CX, FD and AFDmax metrics. Moreover, it confirms that the FA can be explained purely by properties of the fiber configuration and does not necessarily reflect changes in fiber properties, such as myelination.

The FS is a metric that is based solely on second-order statistics of the Bingham distribution. It turned out to be rather unreliable, at least if more than one fiber bundle is present in the voxel (Tab. 2) or if the SNR is not very high (Tab. 1). This finding limits the practical usability of this metric (as well as any other metric based on the second moments of the Bingham distribution). Consequently, the mappings of this metric shown in Fig. 7-9, 11, D.1, D.2 have to be interpreted with great care.

When mapping the bundle specific metrics a bundle correspondence problem arises, that is, between neighboring voxels it is not a priori clear which fODF peaks represent the same fiber bundle. As a result of this problem, the acquired maps for bundles appear less smooth than those of non-bundle specific metrics. The elegant solution to this problem is to map the parameters along single fiber pathways obtained from tractography. The decomposition of the fODF then allows the estimation of metrics along the fibers. This was investigated in the work by Schreiber et al. (2014). In their work a novel tractography method is used for estimating the most probable connection between two regions of interest. Then, bundle dependent metrics like those described here are mapped along the pathways, thereby giving information on the change of the microstructure along distinct fiber bundles. A similar problem arises when bundle

specific metrics need to be compared between subjects (e.g.; Jbabdi et al., 2010, Raffelt et al., 2012a).

While the increase in specificity already provides the means for more accurate investigation of regions with changing FA (or other tensor based measures) there are of course some limits concerning the spatial and angular resolution of this method, imposed by the voxel size and by the angular sampling. Moreover, the use of a constant deconvolution kernel inevitably obscures any changes in fiber properties. Hence, if there is a change in myelination or axonal diameter, this will be projected into changes in fiber density. In order to improve this situation, higher angular and especially spatial resolutions are needed (see e.g. Heidemann et al., 2012). Using multiple b-values and diffusion times does further improve the ability to resolve microstructural properties, such as axonal density and axonal diameter (Assaf and Basser, 2005, Alexander et al., 2010 ).

A different issue, also related to the resolution of the fODF, comes from the use of spherical harmonic representations, which, as with every truncated series expansion, introduces a bias into the reconstruction. This can be seen in the results from the simulated data experiments we conducted. Here a higher order leads to a more accurate recovery of the ground truth used in the simulations. The order one can use, however, is limited by the number of gradient directions (and therefore the amount of information) measured and of course by the signal-to-noise ratio (SNR) (Jones et al., 2013). If the order of the spherical harmonic series expansion is too low, then peaks of certain sharpness (opening angle less than 20°, see Figure 3) cannot be represented accurately. This also leads to crossings at small angles (for eighth order below 50° as shown in Figure 5) not being resolved properly, but rather being interpreted as a single large peak. As shown in Figure 10, the higher order leads to better correlation between ground truth and reconstructed values. However, with real data, stability requirements enforce regularization, which limits the effectively used model order.

The truncation of the spherical expansion also leads to ringing artifacts in terms of negative lobes in the approximation of the (strictly positive) fODF. Together with the negative lobes spurious (positive) peaks appear. This is compensated to a certain degree by CSD, however, the regularization influences the shape of the fODF and may lead to regularization artifacts. The danger here lies not only in the misrepresentation of peaks, but also, the regularization may cause spurious positive peaks to arise. These are particularly dangerous, as these peaks cannot be discerned from peaks caused by the underlying microstructure. The stability and the occurrence of spurious peaks may also be ameliorated by using the damped Richardson-Lucy deconvolution (Dell'Acqua et al., 2007, Parker et al., 2013).

The regularization, while very efficient in suppressing negative lobes, also leads to significant shift in the shape of the fODF (Sotiropoulos et al., 2012; Dell'Acqua et al., 2007). Since the Bingham fitting scheme was demonstrated using CSD as deconvolution method, this can lead to misleading metrics, concerning the ground truth. Overall the question remains which amount of the missmatch between ground truth and fitted

values we observed stems from a missmatch between the SH representation of the fODF and the ground truth. This does not only affect the correlations estimated from the simulations but also may lead to a lack of contrast in the metric maps (Figure 9). However, since the Bingham fitting scheme is independent of the underlying model including a different local model may reduce this effect.

A more fundamental point concerns the use of the SH representation in the spherical deconvolution scheme. Although this basis is very convenient for the calculation, it suffers from substantial limitations concerning its ability to represent the fODF. Especially if the kernel is estimated from voxels with relatively parallel fiber arrangement, such as the corpus callosum, the underlying fODF in these voxels as well as similar ones is per definition a Dirac delta function. In other words, very sharp functions have to be approximated, in particular within the large fiber bundles. On the other hand, the angular resolution of the SH representation is rather limited (as discussed above). Hence, especially for parallel fiber bundles, the SH representation is less than perfect.

## Conclusion

Summarizing the Bingham function based fODF peak characterization is a useful tool for gaining insight into the fiber structure with higher specificity than with the FA. While metrics that primarily rely on the first-order moments of the Bingham distribution can be estimated robustly, those that are based on second-order moments (i.e., FS) are much less reliable, thus limiting their usefulness in practice, at least with the type of data used here. The direct link between the metrics and the fODF especially allows a direct correlation of differences in the metrics to changes in the structural configuration of the fiber configuration. However, this specificity also implies a loss in sensitivity, due to a loss of SNR caused by more complex models. Therefore they are best suited for the investigation of areas where one suspects changes in structure to cause changes in FA. Finally, it should be mentioned that the Bingham characterization is also potentially useful for tractography (Seunarine et al., 2007).

## Appendix A: Spherical harmonics expansion

The particular SH base functions used here have been proposed by Descoteaux et al. (2006). For rank m and order l they are defined as:

$$Y_l^m(\theta,\phi) = \sqrt{\frac{2l+1}{4\,\pi}\,\frac{(l-m)!}{(l+m)!}}\,P_l^m(\cos\theta)\exp(im\phi), \tag{A.1}$$

where $P_l^m$ is the Legendre polynomial of rank m and order l. As the measured diffusion signal within each voxel is naturally positive and symmetric with respect to the origin, only spherical harmonic base functions of even rank have to be considered to represent the fODF. Since these functions are mutually orthogonal by definition, we can use them to define a spherical harmonic base. Using the index $j = \frac{1}{2}(l^2 + l + 2) + m$, the base can be written as:

$$Y_j(\theta,\phi) = \begin{cases} Re\left(Y_l^{|m|}(\theta,\phi)\right), & if\ m > 0 \\ Y_l^m(\theta,\phi), & if\ m = 0 \\ Im\left(Y_l^m(\theta,\phi)\right), & if\ m < 0 \end{cases} \tag{A.2}$$

The fODF obtained from spherical deconvolution is therefore described as a series of coefficients $c_j$ that correspond to base functions $Y_j$. The series expansion can be written as:

$$\Psi(\vec{u}) = \sum_{j=1}^{J} c_j Y_j(\vec{u}), \tag{A.3}$$

with $J = (L+2)(L+1)/2$, where L is the spherical harmonic order at which the series expansion is truncated.

## Appendix B: The meaning of the first SH coefficient

The SH expansion of any square integrable, antipodially symmetric, analytical function on the sphere can be written as (Sneeuw, 1994):

$$f(\theta,\phi) = \sum_{l=0}^{\infty}\sum_{m=0}^{l} g_l^m P_l^m(cos\,\theta)\,cos\,m\phi \tag{B.1}$$

The coefficients $g_l^m$ hereof are defined by the following relation using the index j introduced in Appendix A:

$$g_l^m = \frac{1}{4\pi} \int_0^{2\pi} \int_0^{\pi} f(\theta, \phi) P_l^m(\cos\theta) \cos m\phi \sin\theta \, \mathrm{d}\theta \mathrm{d}\phi. \quad \text{(B.2)}$$

Since $P_0^0(x) = 1$, the first coefficient ($g_1 = g_0^1$) can be computed using:

$$g_1 = \frac{1}{4\pi} \int_0^{2\pi} \int_0^{\pi} f(\theta, \phi) \sin\theta \, \mathrm{d}\theta \mathrm{d}\phi, \quad \text{(B.3)}$$

which corresponds to the integral of $f(\theta, \phi)$ over the sphere. Therefore, in the case of $f(\theta, \phi)$ being the fODF this corresponds to the integral of the fODF over the sphere, which in turn describes the number of fibers within a voxel and therefore the fiber density. As $h_1 = 0$, the coefficient $g_1$ is equal to $c_1$(see Appendix A). Thus the first coefficient of the SH expansion is equal to the fiber density.

## Appendix C: Angular representation of concentration parameters

When viewing the Bingham function as angular function in one of the planes $\overrightarrow{\mu_0} \times \overrightarrow{\mu_1}$ or $\overrightarrow{\mu_0} \times \overrightarrow{\mu_2}$, then we can write it as function of the angle α between the direction for which we want to examine the concentration parameter and the main direction $\overrightarrow{\mu_0}$ (as shown in Figure C.1). Let $k_1$ be the concentration parameter connected to $\overrightarrow{\mu_1}$ and $k_2$ connected to $\overrightarrow{\mu_2}$. As a shorthand we will use $k_{1,2}$ to denote either of these parameters, as the Bingham function is independent of the other as long as viewed in one of the planes separately.

As function of α, the Bingham function reduces to:

$$\beta(\alpha) = f_0 \exp\left(-k_{1,2}(\sin\alpha)^2\right), \tag{C.1}$$

We define the concentration parameter dependent opening angle $\kappa_{1,2}$ as:

$$\kappa_{1,2} = \operatorname{asin}\sqrt{\frac{1}{2\,k_{1,2}}}, \tag{C.2}$$

This angle describes the distance to the main direction at which the function dropped to $\exp(-1/2)$ of its maximum value. This is analogous to the angle at which a Normal distribution reaches 1-sigma level $\left(\mathcal{N}(\sigma) = \frac{1}{\sigma\sqrt{2\pi}}\exp\left(-\frac{1}{2}\right)\right)$. Therefore the angle κ can be seen as the standard deviation angle of the Bingham function.

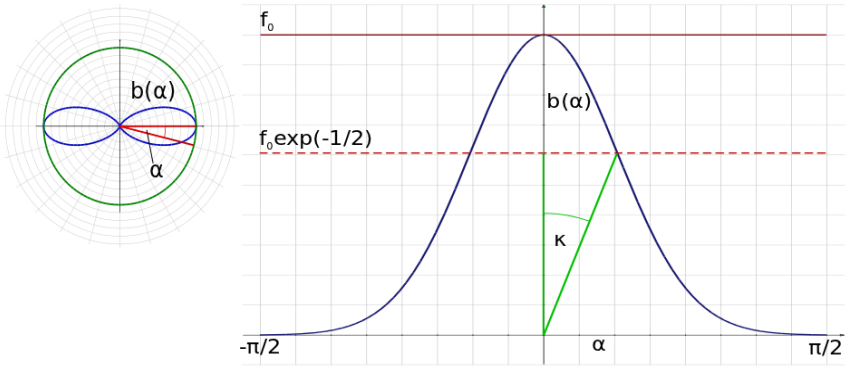


Figure C.1: Derivation of the peak opening angle. On the left the Bingham function is shown in blue as polar plot. The green circle shows the value $f_0$. The angle to the main direction of the Bingham function is noted as α. On the right the Bingham function is shown as function of α in Cartesian coordinates. The angle κ describes the angle at which the function dropped to $\exp(-1/2)$ of its maximum value.

## Appendix D: Unsmoothed metric maps

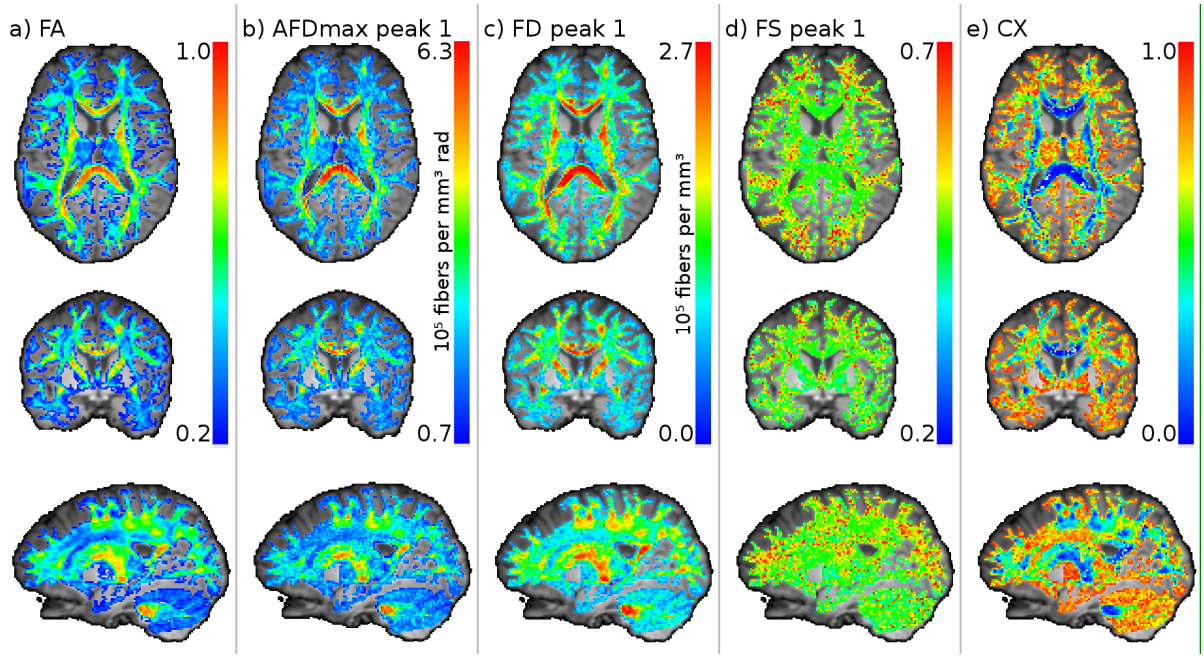


Figure D.1: Unsmoothed metric maps for the first peak, FA and CX. The metrics are mapped onto the white matter by using an FA mask which was thresholded at 0.15 and manually expanded to include the complete white matter and the thalamus. The T1 image is used as background.

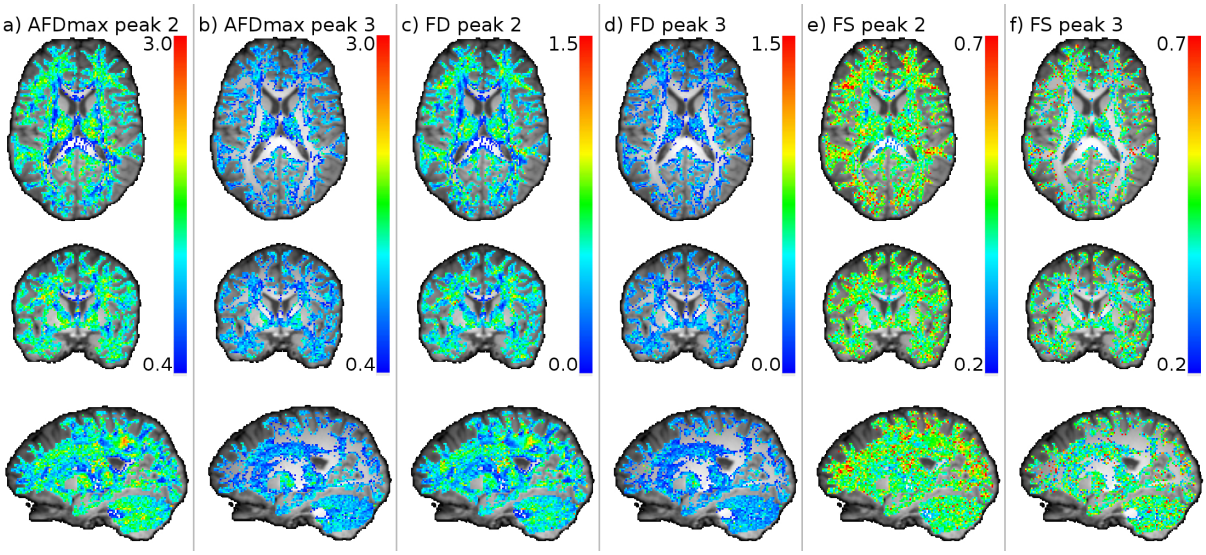


Figure D.2: Unsmoothed metric maps for the second and third peak. The metrics are mapped onto the white matter by using an FA mask which was thresholded at 0.15 and manually expanded to include the complete white matter and the thalamus. The T1 image is used as background.

## Acknowledgements

Part of this work was supported by the FET project CONNECT of the EU (www.brain-connect.eu). The authors want to thank Ralph Schurade for integrating the developed method into BrainGL, an open-source software for analysis and visualization of brain connectivity, available at http://brainGL.googlecode.com.

## References

Aboitiz F, Scheibel AB, Fisher RS, Zaidel E (1992) Fiber composition of the human corpus callosum. Brain Res 598:143-153.

Aganj I, Lenglet C, Sapiro E, Yacoub E, Ugurbil K, Harel N (2010) Reconstruction of the orientation distribution function in single- and multiple-shell q-ball imaging within constant solid angle. Magn Reson Med 64:554-566.

Aja-Fernandez S, Niethammer M, Kubicki M, Shenton ME, Westin C-F (2008) Restoration of DWI data using a Rician LMMSE estimator. IEEE Trans Med Imaging 27:1389-1403.

Alexander D, Hubbard P, Hall M, Moore E, Ptito M, Parker GJM, Dyrby T (2010) Orientationally invariant indices of axon diameter and density from diffusion MRI. Neuroimage 52:1374-1389.

Alexander DC (2005) Maximum entropy spherical deconvolution for diffusion MRI. Inf Process Med Imaging (IPMI), 19:76-87.

Assaf Y, Basser P (2005) Composite hindered and restricted model of diffusion (CHARMED) MR imaging of the human brain. Neuroimage 27:48-58.

Barnett A (2009) Theory of Q-ball imaging redux: Implications for fiber tracking. Magn Reson Med 62:910-923.

Basser P, Mattiello J, Le Bihan D (1994) MR diffusion tensor spectroscopy and imaging. Biophys J 66:259-267.

Basser PJ (1995) Inferring microstructural features and the physiological state of tissues from diffusion-weighted images. NMR Biomed 8:333-344.

Behrens TE, Woolrich MW, Jenkinson M, Johansen-Berg H, Nunes RG, Clare S, Matthews PM, Brady JM, Smith SM (2003) Characterization and propagation of uncertainty in diffusion-weighted MR imaging. Magn Reson Med 50:1077-1088.

Behrens TEJ, Berg HJ, Jbabdi S, Rushworth MFS, Woolrich MW (2007) Probabilistic diffusion tractography with multiple fibre orientations: What can we gain? Neuroimage 34:144-155.

Bingham C (1974) An antipodally symmetric distribution on the sphere. Ann Statist 2:1201-1225.

Caan MWA, Khedoe HG, Poot DHJ, den Dekker AJ, Olabarriaga SD, Grimbergen KA, van Vliet LJ, Vos FM (2010) Estimation of diffusion properties in crossing fiber bundles. IEEE Trans Med Imaging 29:1504-1515.

Callaghan PT, Coy A, Macgowan D, Packer KJ, Zelaya FO (1991) Diffraction-like effects in NMR diffusion studies of fluids in porous solids. Nature 351:467-469.

Canales-Rodríguez E, Melie-García L, Iturria-Medina Y (2009) Mathematical description of q-space in spherical coordinates: Exact q-ball imaging. Magn Reson Med 61:1350-1367.

Conturo TE, Lori NF, Cull TS, Akbudak E, Snyder AZ, Shimony JS, McKinstry RC, Burton H, Raichle ME (1999) Tracking neuronal fiber pathways in the living human brain. Proc Natl Acad Sci U S A 96:10422-10427.

Cory D, G., Garroway A, N. (1990) Measurement of translational displacement probabilities by NMR: An indicator of compartmentation. Magn Reson Med 14:435-444

Dell'Acqua F, Rizzo G, Scifo P, Clarke RA, Scotti G, Fazio F (2007) A model-based deconvolution approach to solve fiber crossing in diffusion-weighted MR imaging. IEEE Trans Biomed Eng 54:462-472.

Dell'Acqua F, Scifo P, Rizzo G, Catani M, Simmons A, Scotti G, Fazio F (2010) A modified damped Richardson-Lucy algorithm to reduce isotropic background effects in spherical deconvolution. Neuroimage 49:1446-1458.

Dell'Acqua F, Simmons A, Williams SCR, Catani M (2013) Can spherical deconvolution provide more information than fiber orientations? Hindrance modulated orientational anisotropy, a true-tract specific index to characterize white matter diffusion. Hum Brain Mapp 34:2464-2483.

Descoteaux M (2008) High angular resolution diffusion MRI: From local estimation to segmentation and Tractography. PhD Thesis. University of Nice. France.

Descoteaux M, Angelino E, Fitzgibbons S, Deriche R (2006) Apparent diffusion coefficients from high angular resolution diffusion imaging: estimation and applications. Magn Reson Med 56:395-410.

Descoteaux M, Deriche R, Knösche TR, Anwander A (2009) Deterministic and probabilistic tractography based on complex fibre orientation distributions. IEEE Trans Med Imaging 28:269-286.

Fillard P, Descoteaux M, Goh A, Gouttard S, Jeurissen B, Malcolm J, Ramirez-Manzanares A, Reisert M, Sakaie K, Tensaouti F, Yo T, Mangin JF, Poupon C (2011) Quantitative evaluation of 10 tractography algorithms on a realistic diffusion MR phantom. Neuroimage 56:220-234.

Ghosh A, Deriche R (2011) Extracting geometrical features & peak fractional anisotropy from the ODF for white matter characterization. IEEE Int Symp Biomed Imag (ISBI), 266-271.

Heidemann RM, Anwander A, Feiweier T, Knösche TR, Turner R (2012) k-space and q-space: Combining ultra-high spatial and angular resolution in diffusion imaging using ZOOPPA at 7T. Neuroimage 60:967-978.

Jbabdi S, Behrens TEJ, Smith SM (2010) Crossing fibres in tract-based spatial statistics. Neuroimage 49:249-256.

Jenkinson M, Bannister P, Brady M, Smith S (2002) Improved optimization for the robust and accurate linear registration and motion correction of brain images. Neuroimage 17:825-841.

Jeurissen B, Leemans B, Tournier J-D, Jones D, Sijbers J (2010) Estimating the number of fiber orientations in diffusion MRI voxels: A constrained spherical deconvolution study. ISMRM 18th annual meeting, 573.

Jian B, Vemuri BC (2007) A unified computational framework for deconvolution to reconstruct multiple fibers from diffusion weighted MRI. IEEE Trans Med Imaging 26:1464-1471.

Jones DK, Knösche TR, Turner R (2013) White matter integrity, fiber count, and other fallacies: The do's and don'ts of diffusion MRI. Neuroimage 73:239-254.

Kaden E, Knösche TR, Anwander A (2007) Parametric spherical deconvolution: Inferring anatomical connectivity using diffusion MR imaging. Neuroimage 37:474-488.

Kreher BW, Schneider JF, Mader I, Martin E, Hennig J, Il'yasov KA (2005) Multitensor approach for analysis and tracking of complex fiber configurations. Magn Reson Med 54:1216-1225.

Le Bihan D, Breton E, Lallemand D, Grenier P, Cabanis E, Laval-Jeantet M (1986) MR imaging of intravoxel incoherent motions: Application to diffusion and perfusion in neurologic disorders. Radiology 161:401-407.

Malcolm JG, Shenton ME, Rathi Y (2010) Filtered multitensor tractography. IEEE Trans Med Imaging 29:1664-1675.

Mardia KV (1975) Statistics of directional data. J Roy Statist Soc. Series B (Methodological), 37:349-393.

Mori S, van Zijl PC (2002) Fiber tracking: Principles and strategies - a technical review. NMR Biomed 15:468-480.

Onstott TC (1980) Application of the Bingham distribution function in paleomagnetic studies. J Geophys Res 85:1500-1510.

Parker GD, Marshall AD, Rosin PL, Drage N, Richmond S, Jones DK (2013) A pitfall in the reconstruction of fibre ODFs using spherical deconvolution of diffusion MRI data. Neuroimage 65:433-448.

Parker GJM, Haroon HA, Wheeler-Kingshott CAM (2003) A framework for a streamline-based probabilistic index of connectivity (PICo) using a structural interpretation of MRI diffusion measurements. J Magn Reson Imaging 18:242-254.

Pasternak O, Assaf Y, Intrator N, Sochen N (2008) Variational multiple-tensor fitting of fiber-ambiguous diffusion-weighted magnetic resonance imaging voxels. Magn Reson Imaging 26:1133-1144.

Poupon C, Rieul B, Kezele I, Perrin M, Poupon F, Mangin JF (2008) New Diffusion Phantoms Dedicated to the Study and Validation of High-Angular-Resolution Diffusion Imaging (HARDI) Models. Magn Reson Med 60:1276-1283.

Raffelt D, Tournier J-D, Crozier S, Connelly A, Salvado O (2012a) Reorientation of fiber orientation distributions using apodized point spread functions. Magn Reson Med 67:844-855.

Raffelt D, Tournier J-D, Rose S, Ridgway GR, Henderson R, Crozier S, Salvado O, Connelly A (2012b) Apparent Fibre Density: A novel measure for the analysis of diffusion-weighted magnetic resonance images. Neuroimage 59:3976-3994.

Scherrer B, Warfield SK (2010) Why multiple b-values are required for multi-tensor models. Evaluation with a constrained log-euclidean model. IEEE Int Symp Biomed Imag (ISBI) 1389-1392.

Schreiber J, Riffert TW, Anwander A, Knösche TR (2014) Plausibility Tracking: A method to evaluate anatomical connectivity and microstructural properties along fiber pathways. Neuroimage 90:163-170.

Schultz T, Kindlmann G (2010) A maximum enhancing higher-order tensor glyph. Comput Graph Forum 29:1143-1152.

Seunarine KK, Cook PA, Hall MG, Embleton KV, Parker GJM, Alexander DC (2007) Exploiting peak anisotropy for tracking through complex structures. IEEE Int Conf Comp Vis 1-8.

Sneeuw N (1994) Global spherical harmonic analysis by least-squares and numerical quadrature methods in historical perspective. Geophys J Int 118:707-716.

Sotiropoulos SN, Behrens TE, Jbabdi S (2012) Ball and rackets: Inferring fiber fanning from diffusion-weighted MRI. Neuroimage 60:1412–1425.

Tabelow K, Voss HU, Polzehl J (2012) Modeling the orientation distribution function by mixtures of angular central Gaussian distributions. J Neurosci Methods 203:200-211.

Takahashi M, Hackney DB, Zhang GX, Wehrli SL, Wright AC, O'Brien WT, Uematsu H, Wehrli FW, Selzer ME (2002) Magnetic resonance microimaging of intraaxonal water diffusion in live excised lamprey spinal cord. Proc Natl Acad Sci U S A 99:16192-16196.

Tanaka H (1999) Circular asymmetry of the paleomagnetic directions observed at low latitude volcanic sites. Earth Planets Space 51:1279-1286.

Tournier JD, Calamante F, Connelly A (2007) Robust determination of the fibre orientation distribution in diffusion MRI: Non-negativity constrained super-resolved spherical deconvolution. Neuroimage 35:1459-1472.

Tournier JD, Calamante F, Connelly A (2012) MRtrix: Diffusion tractography in crossing fiber regions. Int J Imaging Syst Technol 22:53-66.

Tournier JD, Calamante F, Gadian D, Connelly A (2004) Direct estimation of the fiber orientation density function from diffusion-weighted MRI data using spherical deconvolution. Neuroimage 23:1176-1185.

Tristán-Vega A, Westin CF, Aja-Fernández S (2009) Estimation of fiber orientation density probability density functions in high angular resolution diffusion imaging. Neuroimage 47:638-650.

Tuch D (2004) Q-ball imaging. Magn Reson Med 52:1358-1372.

Tuch D, Reese T, Wiegell M, Makris N, Belliveau J, Wedeen V (2002) High angular resolution diffusion imaging reveals intravoxel white matter fiber heterogeneity. Magn Reson Med 48:577-582.

Zhang H, Schneider T, Wheeler-Kingshott CA, Alexander DC (2012) NODDI: Practical in vivo neurite orientation dispersion and density imaging of the human brain. Neuroimage 61:1000-1016.